

Single scattering and effective medium description of multilayer cylinder metamaterials: Application to graphene- and to metasurface-coated cylinders

Charalampos P. Mavidis ^{1,2,*} Anna C. Tasolamprou ^{2,3,†} Eleftherios N. Economou,^{2,4}
Costas M. Soukoulis,^{2,5} and Maria Kafesaki^{1,2}

¹*Department of Materials Science and Technology, University of Crete, 70013 Heraklion, Crete, Greece*

²*Institute of Electronic Structure and Laser, Foundation for Research and Technology Hellas, N. Plastira 100, 70013 Heraklion, Crete, Greece*

³*Section of Electronic Physics and Systems, Department of Materials Science and Technology, University of Crete, Heraklion, Crete, Greece*

⁴*Department of Physics, University of Crete, Heraklion, Greece*

⁵*Ames Laboratory and Department of Physics and Astronomy, Iowa State University, Ames, Iowa 50011, USA*



(Received 9 February 2023; revised 7 April 2023; accepted 8 April 2023; published 27 April 2023)

Coated and multicoated cylinder systems constitute an appealing metamaterial category, as they allow a very rich and highly tunable response, resulting from the interplay of the many different geometrical and material parameters involved. Here we derive and propose an effective medium approach for the detailed description and analysis of the electromagnetic wave propagation in such systems. In particular, we investigate infinitely-long multilayered cylinders with additional electric and magnetic surface conductivities at each interface. Our effective medium approach is based on the well known in the solid state physics community coherent potential approximation (CPA) method, combined with a transfer matrix-based formulation for cylindrical waves. Employing this effective medium scheme, we investigate two realistic systems, one comprising of cylindrical tubes made of uniform tunable graphene sheets and one of cylinders/tubes formed of metasurfaces exhibiting both electric and magnetic sheet conductivities. Both systems show a rich palette of engineerable electromagnetic features, including tunable hyperbolic response, double negative response, and ϵ -near-zero and μ -near-zero response regions.

DOI: [10.1103/PhysRevB.107.134120](https://doi.org/10.1103/PhysRevB.107.134120)

I. INTRODUCTION

Electromagnetic metamaterials are artificial, structured materials comprising of subwavelength resonant building blocks, the meta-atoms. Due to their versatile nature, metamaterials offer the possibility of novel and unconventional electromagnetic wave control, and thus advancements in a large variety of wave-control-related applications, including imaging, sensing, communications, etc. [1–4]. Metamaterials' exceptional electromagnetic properties stem to a larger degree from the architecture of the meta-atoms; through this architecture, the distribution of the local currents excited by an impinging electromagnetic wave is engineered, providing the desired response. Particularly known forms of meta-atoms are properly aligned metallic short wires, behaving as macroscopic resonant electric dipoles and producing a resonant electric response (resonant permittivity), and metallic split ring resonators, leading to resonant circulating currents and the emergence of a resonant magnetic response [5]. Another approach to create resonant electric and/or magnetic response is by exploiting the Mie-based resonances in high index dielectric (or semiconducting) meta-atoms; this approach is typically proposed for applications in high (IR and optical) frequencies [6–8], where metals experience detrimentally high losses. Through tunable resonant magnetic

and/or electric response one can engineer a plethora of different and peculiar metamaterial properties, such as negative, near-zero permittivity and/or permeability, negative refractive index, peculiar anisotropy, asymmetric effects and many more [9–12] (Note that because of the subwavelength meta-atom size metamaterials provide homogeneous-medium-like (effective) properties and response).

Besides bulk (three-dimensional) metamaterials, many additional exciting functionalities stem from the electromagnetic wave interaction with thin meta-atom layers, known as metasurfaces, which attract a constantly growing research attention. Metasurfaces, by allowing modulation of the meta-atoms along them, allow the engineering of both phase and amplitude of the electromagnetic fields impinging on them, acquiring thus the ability to replace bulk, heavy and difficult to use conventional optical elements (mirrors, lenses, etc.). Due to their ultrathin nature and the subwavelength meta-atom size, metasurfaces can be conveniently described as effective electromagnetic sheets [13], through appropriate sheet conductivities. Metasurfaces comprising of a thin layer sustaining orthogonal electric and magnetic dipoles have been utilized for applications as reflect-arrays, transmit-arrays, holographic surfaces and others [14]. Moreover, metasurfaces' fine electromagnetic features have been shown to enable enhanced detection and sensing, thin film polarizers, shielding, beam shaping and other useful functionalities [15–21].

As mentioned, metamaterials and metasurfaces can be made of metallic, dielectric or semiconducting components. They can be also made of a combination of dielectric,

*mavidis@iesl.forth.gr

†atasolam@iesl.forth.gr

semiconducting and metallic parts in a properly designed meta-atom architecture and cluster arrangement. A scheme that has gained significant popularity is structures composed of coated (or even multicoated) cylinders or spheres. Such structures are characterized by a relatively straightforward design and have been proposed for a variety of applications due to the increased degree of design freedom related to the thicknesses and constituent materials in each layer. With proper selection of geometry and materials, coated cylinders or spheres can lead to overlapping of different resonances, which is crucial in metasurfaces since it can offer full transmission or reflection and 2π phase modulation (allowing in principle arbitrary wavefront control), resonances with engineered quality factors, etc. Applications of such structures include superscattering [22–27], electromagnetic cloaking [25,28–35], lenses and many others [36]. Moreover, metamaterials made of cylindrical meta-atoms, which are the system of interest in the present work, are inherently anisotropic, allowing the possibility of hyperbolic dispersion relation and anisotropic negative or near-zero refractive index [37]. Such structures can be experimentally realized following the progress of micro and nanotechnology; for example emerging technologies focused on the implementation of carbon nanotubes have given already metamaterial and photonic crystal orientated developments [38–41]. Even more interesting electromagnetic features can occur in cylindrical meta-atoms coated with tunable sheets bearing individual electric and/or magnetic resonances to be combined with the response of the coated atom. Such coatings may involve, for example, a 2D material, like uniform graphene or structured (patterned) graphene, or an electromagnetically thin sheet of cut wires or split ring resonators [28,34,42–44], e.g., in a flexible metasurface implementation [45,46]. It should be mentioned here that graphene in particular, either in a patterned metasurface form or as a uniform sheet, is very appealing as a coating material due to its intrinsic ultrathin nature and the exceptionally tunable electromagnetic properties, especially in the THz wavelengths where its EM behavior is dominated by a Drude-like response [47–50].

It is clear that an analytical assessment of the electromagnetic response of coated and multicoated cylinder-based metamaterial structures is important, as it gives the possibility for the in-depth understanding of the physical mechanisms that lead to the resonant structure response, and, subsequently, for engineering of this response through structure engineering and optimization, targeting advanced electromagnetic functionalities and applications. Assemblies of resonant cylinders can be treated as an effective homogeneous material in the limit of small characteristic lengths (radius, unit cell size) compared to the wavelength of interest and (in most of the cases) in the far-field limit. Homogenization approaches applied in systems of coated spheres and cylinders have shown that coatings can provide many interesting effects, as for example an increased bandwidth of negative permittivity and permeability in comparison with their noncoated counterparts [51]. However, to our knowledge, an analytic homogenization approach that can incorporate an arbitrary number (larger than one) of coatings for each cylinder has not been reported in the literature yet. Additionally, although the scattering properties of cylinders and spheres coated with graphene metasurfaces

have been quite extensively studied, coatings/sheets showing arbitrary resonant electric and/or resonant magnetic response (representing more complex metasurface-coatings and allowing delicate interplay of electric and magnetic dipoles, resulting to additional advanced functionalities) [52–59] are much less explored.

The aim of this work is to develop a framework/formalism to analyze in detail the resonant behavior and wave propagation in systems of multilayer cylinders coated also with conducting sheets (metasurfaces) of both electric and magnetic response, as well as to apply this framework to cases of high foreseen theoretical or practical interest. Towards this direction, we derive an homogeneous effective medium approach for systems of infinitely-long multilayer cylinders, with an arbitrary number of layers (coatings; of metallic, high-index dielectric or even resonant materials) and with the incorporation of both electric and magnetic sheet conductivities at each interface (i.e., between coatings). Our homogenization approach is based on the well known in the solid state physics community coherent potential approximation, CPA [60–64], suitable also quite beyond the long-wavelength limit. To calculate the single cylinder scattering amplitudes for the multilayer cylinders, which is an essential step in the CPA application, we develop a Transfer Matrix Method (TMM) for cylindrical waves, connecting the wave amplitudes at the different layers. We apply the developed formalism in two different systems/metamaterials: (i) of cylinders (nanotubes) of uniform graphene sheets, with tunable response and (ii) of cylinders formed of metasurfaces with arbitrary electric and magnetic resonances in the metasurface conductivity. In both systems, we study the single meta-atom (multicoated cylinder) scattering and the effective medium response, which unveils the existence of rich electromagnetic features, i.e., controllable hyperbolic response of both types I and II, double negative response, and epsilon-near-zero and mu-near-zero response. The paper is organized as follows. In Sec. II we present our method, i.e., starting from the single meta-atom scattering we derive the relations for the effective electric permittivity and magnetic permeability tensor components for the corresponding metamaterial. In Secs. III A and III B, we apply the method in systems of single- and double-layer/wall cylindrical nanotubes made of (a) tunable graphene sheets and (b) metasurfaces with both electric and magnetic surface conductivity. The first case approximates systems of single and double-wall carbon nanotubes, which are systems of high technological interest. The second system can approximate, among others, metamaterials of cylinders coated with a structured 2D material, e.g., graphene, transition metal dichalcogenide monolayers, etc. In both cases, we demonstrate the engineerable effective electric permittivity and magnetic permeability response, leading to the emergence of various interesting optical phases and possibilities. Finally we present the conclusions on our work.

II. METHODS

We begin our analysis from the methods derived and employed in this work for the system shown in Fig. 1. In the first part, we present the THz electric and magnetic sheet

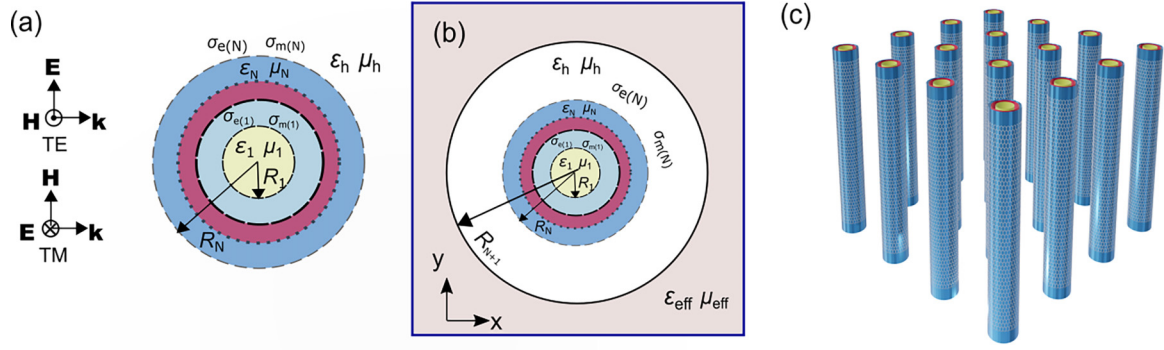


FIG. 1. (a) Top view schematic of the more general meta-atom geometry investigated in this work: A cylinder of N concentric bulk layers, separated by metasurfaces. Each bulk layer is characterized by relative electric permittivity ϵ_ℓ and magnetic permeability μ_ℓ . The interface between the ℓ th and the $(\ell + 1)$ th layer is coated with a metasurface with electric conductivity $\sigma_{e(\ell)}$ and magnetic conductivity $\sigma_{m(\ell)}$. The polarization definition is also shown, where we assume normal incidence. (b) Schematic of the setup for the effective medium derivation. The original cylinder [of panel (a)] is coated with a cylindrical layer of the host material (white color), with radius $R_{N+1} = R_N/\sqrt{f}$, where f is the filling ratio of the cylinders in the metamaterial under investigation, and is embedded in the homogeneous effective medium under determination (with relative permittivity ϵ_{eff} and permeability μ_{eff}). (c) Three-dimensional view of the metamaterial under investigation: an array of multilayered cylinders.

conductivities of the metasurfaces considered in the application cases discussed here. In the second part we present first the derivation of a transfer matrix method, which allows us to calculate the scattering properties of a cylinder composed of N cocentered layers of different materials, with metasurfaces at the interfaces of these layers. Next, we derive the CPA-based effective medium model for two-dimensional arrays of such multilayered cylinders, based on the single scattering calculations.

A. 2D conductivities

In this section, we present the electromagnetic properties of the 2D sheets/coatings of the examples considered in this work, i.e., the uniform graphene sheet and the metasurface exhibiting both electric and magnetic resonance.

For the graphene case, the conductivity σ_g as a function of the Fermi energy E_F and the temperature T was obtained by Kubo formula, derived in the context of rapid phase approximation (RPA) [65]; it reads as

$$\sigma_g(\omega) = \sigma_{\text{intra}} + \sigma_{\text{inter}}, \quad (1)$$

where the intraband contribution is

$$\sigma_{\text{intra}}(\omega) = \frac{2e^2 k_B T}{\pi \hbar^2} \frac{i}{\omega + i\tau^{-1}} \ln \left[2 \cosh \left(\frac{E_F}{2k_B T} \right) \right] \quad (2)$$

and the interband contribution is

$$\sigma_{\text{inter}}(\omega) = \frac{e^2}{4\hbar} \left\{ \frac{1}{2} + \frac{1}{\pi} \arctan \left(\frac{\hbar\omega - 2E_F}{2k_B T} \right) - \frac{i}{2\pi} \ln \left[\frac{(\hbar\omega + 2E_F)^2}{(\hbar\omega - 2E_F)^2 + (2k_B T)^2} \right] \right\}. \quad (3)$$

Here ω is the angular frequency, $\hbar = 1.055 \times 10^{-34}$ J s the reduced Planck constant, $k_B = 1.38 \times 10^{-23}$ J K $^{-1}$ the Boltzmann constant, $e = 1.602 \times 10^{-19}$ C the electron charge and τ the electrons' relaxation time. Unless otherwise stated, in this paper we use a Fermi level $E_F = 0.2$ eV and a typical relaxation time $\tau = 1$ ps. The real and imaginary parts of the

graphene conductivity for these values and for our frequency region of interest are shown in Fig. 2(a).

Regarding the metasurface coatings employed, usually in the literature their response is approximated by a sheet material with effective electric and magnetic 2D conductivities consisting of a summation of Lorentzian resonances

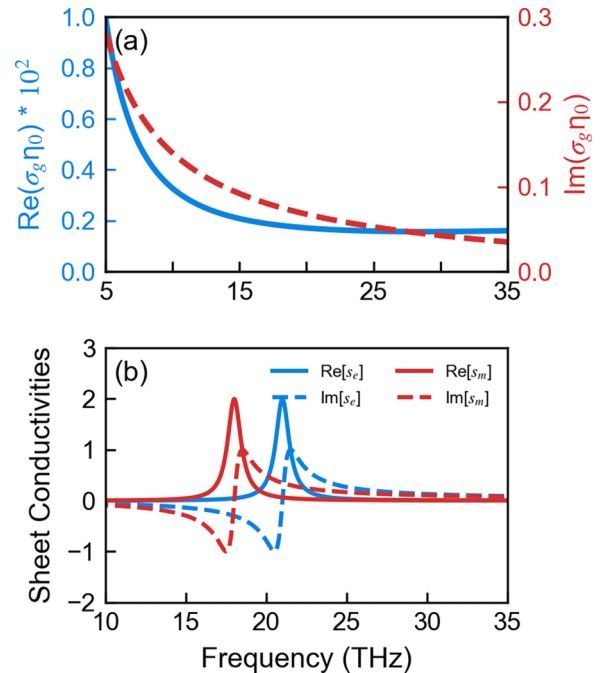


FIG. 2. (a) Real part (times 100) (left axis, blue line) and imaginary part (right axis, red line) of the sheet conductivity of a uniform graphene sheet modelled by Eq. (1), assuming Fermi level $E_F = 0.2$ eV and relaxation time $\tau = 1$ ps. (b) Normalized real (solid lines) and imaginary (dashed lines) parts of electric (s_e) and magnetic (s_m) sheet conductivities calculated using Eqs. (4) and (5), assuming parameters $\omega_e/2\pi = 21$ THz, $\Gamma_e/2\pi = \Gamma_m/2\pi = 2$ THz, $\kappa_e/2\pi = \kappa_m/2\pi = 1$ THz, and $\omega_m/2\pi = 18$ THz; for the definition of those parameters see main text. η_0 is the free-space impedance.

[57–59,66,67]. To simplify our analysis we consider here a metasurface with isotropic surface conductivities and a single electric and magnetic resonance:

$$s_e = \sigma_e \eta_0 = \frac{i\kappa_e \omega}{\omega^2 - \omega_e^2 + i\omega\Gamma_e}, \quad (4)$$

$$s_m = \frac{\sigma_m}{\eta_0} = \frac{i\kappa_m \omega}{\omega^2 - \omega_m^2 + i\omega\Gamma_m}, \quad (5)$$

where η_0 is the free-space impedance, $\omega_{e/m}$ are the resonance frequencies, $\kappa_{e/m}$ and $\Gamma_{e/m}$ are parameters of the Lorentzians. For the purpose of the present analysis we have chosen the values of the parameters involved in the conductivities as $f_e = \omega_e/2\pi = 21$ THz, $\Gamma_e/2\pi = \Gamma_m/2\pi = 1$ THz, $\kappa_e/2\pi = \kappa_m/2\pi = 2$ THz, and $f_m = \omega_m/2\pi = 18$ THz. The real and imaginary part of the corresponding electric and magnetic conductivities are shown in Fig. 2(b).

B. Single scattering

Having defined the sheet conductivities of the graphene and metasurface coatings, we move to the investigation of a single cylinder system. We consider an infinitely-long cylinder consisting of N cocentered layers. The system is shown in Fig. 1(a). The ℓ th layer is characterized by its thickness $\Delta_\ell = R_\ell - R_{\ell-1}$ ($R_0 = 0$), where R_ℓ is the distance from the center to the perimeter of the ℓ th layer; its relative electric permittivity is ε_ℓ , the relative magnetic permeability is μ_ℓ , the electric surface conductivity is $\sigma_{e(\ell)}$ and the magnetic surface conductivity is $\sigma_{m(\ell)}$. The cylinder is embedded in a host material with relative electric permittivity ε_h and magnetic permeability μ_h . We consider wave propagation perpendicular to the cylinder axis. Since the cylinder is infinitely-long and there is no propagation component parallel to its axis, the problem is two dimensional and can be decoupled into two separate polarizations, the transverse electric (TE), with the electric field normal to the cylinder axis, and the transverse magnetic (TM) polarization, with the magnetic field normal to the cylinder axis. In each layer, the fields can be expanded on the basis of cylindrical vector harmonics. In the ℓ th layer the field $\mathbf{F} = \{\mathbf{E}, \mathbf{H}\}$ (electric or magnetic) parallel to the cylinder axis (z direction) will be

$$\mathbf{F}_\ell \sim \sum_\nu [c_{\ell\nu} \mathbf{N}_{\nu k_\ell}^{(\text{outward})} + d_{\ell\nu} \mathbf{N}_{\nu k_\ell}^{(\text{inward})}], \quad (6)$$

with $\mathbf{N}_{\nu k_\ell}^{(\text{outward})} \sim H_\nu(k_\ell r)$ and $\mathbf{N}_{\nu k_\ell}^{(\text{inward})} \sim J_\nu(k_\ell r)$ standing for the outgoing and ingoing cylindrical harmonics respectively [68]. The functions $J_\nu(\cdot)$ and $H_\nu(\cdot)$ are the Bessel and the first kind Hankel function of order ν , and $k_\ell = \sqrt{\varepsilon_\ell \mu_\ell} \omega/c$. The expansion coefficients $c_{\ell\nu}$ and $d_{\ell\nu}$ can be calculated by imposing the appropriate boundary conditions at the interface $r = R_\ell$ [69–71]:

$$\hat{\rho} \times [\mathbf{E}_{\ell+1} - \mathbf{E}_\ell] = -\mathbf{j}_{m(\ell)} = -\sigma_{m(\ell)} \frac{\mathbf{H}_\ell + \mathbf{H}_{\ell+1}}{2}, \quad (7)$$

$$\hat{\rho} \times [\mathbf{H}_{\ell+1} - \mathbf{H}_\ell] = \mathbf{j}_{e(\ell)} = \sigma_{e(\ell)} \frac{\mathbf{E}_\ell + \mathbf{E}_{\ell+1}}{2}, \quad (8)$$

where $\hat{\rho}$ is the unit vector along the radial direction. Here we have chosen a set of Bessel functions for our descriptions that is not linearly independent, i.e., $J_\nu(\cdot)$ and $H_\nu(\cdot)$ instead of $J_\nu(\cdot)$ and $Y_\nu(\cdot)$ that are commonly used in the literature, because

it is more convenient for the effective medium description in Sec. II C.

By applying the boundary conditions, Eqs. (7) and (8), at each of the interfaces of the N layers of the cylinder, we construct a matrix equation which connects the fields in the innermost layer with the fields outside the cylinder (incident plus scattered field), for each cylindrical wave/harmonic (ν) excited. This transfer matrix equation reads

$$\mathbb{M}_{(N),\nu}^{\mathbf{P}} \begin{pmatrix} b_\nu \\ 0 \end{pmatrix} = \begin{pmatrix} 1 \\ a_\nu \end{pmatrix}, \quad (9)$$

where $\mathbb{M}_{(N),\nu}^{\mathbf{P}}$ is the total transfer matrix for polarization $\mathbf{P} = \{\text{TE}, \text{TM}\}$. With $a_\nu \equiv c_{(N+1),\nu}$ we denote the scattering coefficient of the scattered wave (for coefficient $1 \equiv d_{(N+1),\nu}$ of the incident wave) and with $b_\nu = d_{1\nu}$ the coefficient (inwards) for the core (innermost) layer, while ν stands for the excited mode (cylindrical harmonic).

The total transfer matrix $\mathbb{M}_{(N),\nu}^{\mathbf{P}}$ is derived through the transfer matrices connecting the fields at neighboring layers. For polarization $\mathbf{P} = \{\text{TE}, \text{TM}\}$, the transfer matrix $\mathbb{T}_{\ell\nu}^{\mathbf{P}}$ which transfers the fields from the (ℓ)th layer to the fields in the ($\ell + 1$)th layer can be written as

$$\mathbb{T}_{\ell\nu}^{\mathbf{P}} \begin{pmatrix} d_{\ell\nu} \\ c_{\ell\nu} \end{pmatrix} = \begin{pmatrix} d_{(\ell+1),\nu} \\ c_{(\ell+1),\nu} \end{pmatrix}. \quad (10)$$

For TE polarization, the matrix $\mathbb{T}_{\ell\nu}^{\text{TE}}$ has the form

$$\mathbb{T}_{\ell\nu}^{\text{TE}} = [\mathbb{D}_{(\ell+1)\nu}^{\text{TE}}(R_\ell)]^{-1} \cdot [\mathbb{X}_\ell^+]^{-1} \cdot \mathbb{X}_\ell^- \cdot \mathbb{D}_{\ell\nu}^{\text{TE}}(R_\ell), \quad (11)$$

where

$$\mathbb{D}_{\ell\nu}^{\text{TE}}(R_\ell) = \begin{pmatrix} J'_\nu(k_\ell R_\ell) & H'_\nu(k_\ell R_\ell) \\ \frac{1}{\eta_\ell} J_\nu(k_\ell R_\ell) & \frac{1}{\eta_\ell} H_\nu(k_\ell R_\ell) \end{pmatrix} \quad (12)$$

and the surface conductivity matrices (\mathbb{X}) are

$$\mathbb{X}_\ell^\pm = \begin{pmatrix} 1 & \pm i\sigma_{m(\ell)}/2\eta_0 \\ \mp i\sigma_{e(\ell)}\eta_0/2 & 1 \end{pmatrix}, \quad (13)$$

where $\eta_\ell = \sqrt{\mu_\ell/\varepsilon_\ell}$ is the impedance of the ℓ th layer and $\eta_0 = \sqrt{\mu_0/\varepsilon_0}$ is the vacuum impedance.

For TM polarization, we get

$$\mathbb{T}_{\ell\nu}^{\text{TM}} = [\mathbb{D}_{(\ell+1)\nu}^{\text{TM}}(R_\ell)]^{-1} \cdot [\mathbb{X}_\ell^-]^{-1} \cdot \mathbb{X}_\ell^+ \cdot \mathbb{D}_{\ell\nu}^{\text{TM}}(R_\ell), \quad (14)$$

$$\mathbb{D}_{\ell\nu}^{\text{TM}}(R_\ell) = \begin{pmatrix} J_\nu(k_\ell R_\ell) & H_\nu(k_\ell R_\ell) \\ \frac{1}{\eta_\ell} J'_\nu(k_\ell R_\ell) & \frac{1}{\eta_\ell} H'_\nu(k_\ell R_\ell) \end{pmatrix}. \quad (15)$$

The details of the calculations are presented in Appendix A 1.

The total transfer matrix reads as

$$\mathbb{M}_{(N),\nu}^{\mathbf{P}} = \prod_{\ell=N}^1 \mathbb{T}_{\ell\nu}^{\mathbf{P}}. \quad (16)$$

From Eq. (9) we can calculate the coefficients b_ν (of the field in the core layer) and a_ν (scattered field coefficient) as

$$b_\nu = \frac{1}{\mathbb{M}_{(N),\nu}^{(11)}}, \quad (17)$$

$$a_\nu = \mathbb{M}_{(N),\nu}^{(21)} b_\nu = \frac{\mathbb{M}_{(N),\nu}^{(21)}}{\mathbb{M}_{(N),\nu}^{(11)}}. \quad (18)$$

The scattering and extinction efficiencies of the whole cylinder can all be written in terms of a_ν as

$$Q_{\text{ext}}^{\text{P}} = -\frac{2}{|k_h R_N|} \text{Re} \left[a_0^{\text{P}} + 2 \sum_{\nu=1}^{\infty} a_\nu^{\text{P}} \right], \quad (19)$$

$$Q_{\text{sc}}^{\text{P}} = \frac{2}{|k_h R_N|} \left[|a_0^{\text{P}}|^2 + 2 \sum_{\nu=1}^{\infty} |a_\nu^{\text{P}}|^2 \right]. \quad (20)$$

Limiting expressions for a metasurface-covered cylinder. Having the above equations, one can derive limiting expressions for different systems of practical or theoretical interest. Here, we derive expressions for the resonance frequencies (poles) of the $\nu = 1$ mode of a single-layer cylinder coated with a metasurface. For a single cylindrical layer ($N = 1$) with radius $R_1 = R$ coated with a surface with conductivities σ_e and σ_m in a host material with electric permittivity ε_h and magnetic permeability μ_h , the scattering coefficients will be given based on Eq. (18). In the limit $k_h R \ll 1$ and ignoring terms containing the product term $\sigma_e \sigma_m$, the poles of the TE₁ mode can be found from the expression

$$\frac{1}{\eta_1} \frac{J_1(k_1 R)}{J_1'(k_1 R)} = \frac{\sigma_e \eta_0 \eta_h - i k_h R}{i \eta_h + k_h R \sigma_m \eta_0^{-1}}. \quad (21)$$

Further, if we take the quasistatic limit of $k_h R \ll 1$ and $k_1 R \ll 1$, we find

$$\varepsilon_1 \frac{\omega}{c} R = \frac{i \sigma_e \eta_0 + \varepsilon_h \frac{\omega}{c} R}{\varepsilon_h i \sigma_m \eta_0^{-1} \frac{\omega}{c} R - 1} \quad (22)$$

or

$$\varepsilon_1 \varepsilon_h i \sigma_m \eta_0^{-1} \left(\frac{\omega}{c} R \right)^2 - (\varepsilon_1 + \varepsilon_h) \frac{\omega}{c} R = i \sigma_e \eta_0. \quad (23)$$

For the sake of our analysis, we ignore the damping term in the conductivities [see Eqs. (4) and (5)], i.e., we consider

$$s_{e/m} = \frac{i \kappa_{e/m} \omega}{\omega^2 - \omega_{e/m}^2}. \quad (24)$$

For $x = k_0 R = \omega R/c \ll 1$, we can write the magnetic sheet conductivity as $s_m = \sigma_m \eta_0^{-1} \simeq i \kappa_m (-c/R) \cdot x/\omega_m^2 - (c/R)^3 \cdot x^3/\omega_m^4 + \mathcal{O}(x^4)$, and hence, can ignore the first term of Eq. (23). In this case, we can use Eqs. (23) and (24) to get

$$-(\varepsilon_1 + \varepsilon_h) \frac{\omega}{c} R = i \frac{\kappa_e \omega}{\omega^2 - \omega_e^2}, \quad (25)$$

$$-(\varepsilon_1 + \varepsilon_h) \frac{\omega}{c} R (\omega^2 - \omega_e^2) = -\kappa_e \omega, \quad (26)$$

or

$$(\varepsilon_1 + \varepsilon_h) \frac{R}{c} (\omega^2 - \omega_e^2) = \kappa_e. \quad (27)$$

Finally we find that the frequency of the TE₁ resonance of the structure is at

$$\omega_{\text{TE}_1}^2 \simeq \omega_e^2 + \frac{c \kappa_e}{(\varepsilon_1 + \varepsilon_h) R}. \quad (28)$$

An equivalent expression can be obtained for the TM₁ resonance:

$$\omega_{\text{TM}_1}^2 \simeq \omega_m^2 + \frac{c \kappa_m}{(\mu_1 + \mu_h) R}. \quad (29)$$

For graphene, if we ignore the interband conductivity term in Eq. (1), the sheet conductivity takes the form $\sigma_g(\omega) \simeq$

$i \kappa_g / \omega$, where $\kappa_g = \frac{2e^2 k_B T}{\pi \hbar^2} \ln[2 \cosh(\frac{E_F}{2k_B T})]$; we then get a $1/\sqrt{R}$ dependence of the TE₁ mode resonance frequency.

C. Effective medium theory

In this section, we derive the components of the effective permittivity and permeability tensors for a uniaxial anisotropic system/metamaterial of infinitely-long parallel circular multicoated cylinders of N layers each and surface electric and magnetic conductivities at each cylinder interface.

We follow the same approach as the one of Refs. [62,64], where (in Ref. [64]), we calculated the effective medium parameters for a cluster of cylinders without coating and surface conductivities. To derive the effective medium equations in the case of N -coated cylinders we consider a cylinder of $N+1$ layers embedded in the effective medium, as depicted in Fig. 1(b), and we require the vanishing of the scattering amplitudes. The $(N+1)$ th layer of that cylinder is the host of the original system (with $\varepsilon_{N+1} = \varepsilon_h$ and $\mu_{N+1} = \mu_h$) with thickness $R_{N+1} - R_N$. The radius R_{N+1} of the outer layer is determined by the filling ratio, f , of the cylinders in the original system, as $f = R_N^2/R_{N+1}^2$, i.e., the host-coated cylinder preserves the filling ratio of the original system/metamaterial. The host material (effective medium) in the configuration of Fig. 1(b) has permittivity $\varepsilon_{\text{eff}} = \varepsilon_{\text{eff}}^\perp (\hat{x}\hat{x} + \hat{y}\hat{y}) + \varepsilon_{\text{eff}}^\parallel \hat{z}\hat{z}$ and permeability $\mu_{\text{eff}} = \mu_{\text{eff}}^\perp (\hat{x}\hat{x} + \hat{y}\hat{y}) + \mu_{\text{eff}}^\parallel \hat{z}\hat{z}$ (the symbols \parallel, \perp are defined relative to the cylinders axes, i.e., for ε^\parallel (μ^\parallel) electric (magnetic) field is parallel to the axes of the cylinders). In order to derive the expressions for the tensor components of the effective permittivity and permeability we require that the scattering coefficients of the scattered field in the effective medium, $a_\nu^{\text{(eff)}}$, for both TE and TM polarizations vanish. After algebraic manipulations (see details in Appendix B), this requirement leads to expressions for the coefficients of the original cylinder, which read as

$$a_\nu^{\text{P}}(R_{N+1}; \text{eff}, h) = a_\nu^{\text{P}}(\{R_1, \dots, R_N\}; \{A_1, \dots, A_N\}, h), \quad (30)$$

where $a_\nu^{\text{P}}(R_{N+1}; \text{eff}, h)$ are the scattering coefficients of a single-layered cylinder with electric permittivity ε_{eff} , magnetic permeability μ_{eff} and radius R_{N+1} , embedded in a host with electric permittivity ε_h and magnetic permeability μ_h . In the right-hand-side of Eq. (30), $a_\nu^{\text{P}}(\{R_1, \dots, R_N\}; \{A_1, \dots, A_N\}, h)$ are the scattering coefficients of the original cylinder, consisting of N cocentered layers with radii $\{R_1, R_2, \dots, R_N\}$ and materials (including surface conductivities at each interface) $\{A_1, A_2, \dots, A_N\}$ embedded in the host material (of the original system). In the metamaterial frequency range, $k_h R_{N+1} < 1$, however, there are only two dominant modes per polarization, the lower order ones, i.e., the $\nu = 0$ and the $\nu = 1$ mode. In the limit $k_{\text{eff}} R_{N+1} \ll 1$, we can replace the Bessel functions in Eq. (30) with their limiting expressions assuming small arguments [72]. Considering only the $\nu = 0$ and $\nu = 1$ modes per polarization, we can obtain semi-analytical expressions for all the components of the effective electric permittivity and magnetic permeability tensors, which read as

$$\varepsilon_{\text{eff}}^\parallel = -\frac{2\varepsilon_h}{k_h R_{N+1}} \left[\frac{J_0'(k_h R_{N+1}) + H_0'(k_h R_{N+1}) a_0^{\text{TM}}}{J_0(k_h R_{N+1}) + H_0(k_h R_{N+1}) a_0^{\text{TM}}} \right], \quad (31)$$

$$\mu_{\text{eff}}^{\perp} = \frac{\mu_h}{k_h R_{N+1}} \left[\frac{J_1(k_h R_{N+1}) + H_1(k_h R_{N+1}) a_1^{\text{TM}}}{J_1'(k_h R_{N+1}) + H_1'(k_h R_{N+1}) a_1^{\text{TM}}} \right], \quad (32)$$

$$\mu_{\text{eff}}^{\parallel} = -\frac{2\mu_h}{k_h R_{N+1}} \left[\frac{J_0'(k_h R_{N+1}) + H_0'(k_h R_{N+1}) a_0^{\text{TE}}}{J_0(k_h R_{N+1}) + H_0(k_h R_{N+1}) a_0^{\text{TE}}} \right], \quad (33)$$

$$\varepsilon_{\text{eff}}^{\perp} = \frac{\varepsilon_h}{k_h R_{N+1}} \left[\frac{J_1(k_h R_{N+1}) + H_1(k_h R_{N+1}) a_1^{\text{TE}}}{J_1'(k_h R_{N+1}) + H_1'(k_h R_{N+1}) a_1^{\text{TE}}} \right], \quad (34)$$

where the coefficients a_0^{TE} , a_1^{TE} , a_0^{TM} , a_1^{TM} are the scattering coefficients of the original N -layer cylinder embedded in the host of the original system [the ones of the right-hand side (r.h.s.) of Eq. (30)]. Equations (31) and (34) have the same form as the relations obtained in Ref. [64]. Finally, if we further take the limit $k_h R_{N+1} \ll 1$, we get

$$\varepsilon_{\text{eff}}^{\parallel} = \varepsilon_h \left[1 - \frac{f}{(k_h R_N)^2} \frac{4i}{\pi} a_0^{\text{TM}} \right], \quad (35)$$

$$\mu_{\text{eff}}^{\perp} = \mu_h \left[\frac{(k_h R_N)^2 - f \frac{4i}{\pi} a_1^{\text{TM}}}{(k_h R_N)^2 + f \frac{4i}{\pi} a_1^{\text{TM}}} \right], \quad (36)$$

$$\mu_{\text{eff}}^{\parallel} = \mu_h \left[1 - \frac{f}{(k_h R_N)^2} \frac{4i}{\pi} a_0^{\text{TE}} \right], \quad (37)$$

$$\varepsilon_{\text{eff}}^{\perp} = \varepsilon_h \left[\frac{(k_h R_N)^2 - f \frac{4i}{\pi} a_1^{\text{TE}}}{(k_h R_N)^2 + f \frac{4i}{\pi} a_1^{\text{TE}}} \right], \quad (38)$$

where f is the cylinders filling ratio in the system/metamaterial. Note here that for cylinders without any coating ($N = 1$, $\sigma_e = 0$, $\sigma_m = 0$) in the quasistatic limit (i.e., $k_h R_{N+1} \ll 1$, $k_1 R \ll 1$), Eqs. (31)–(34) reduce to the well-known Maxwell-Garnett expressions.

III. RESULTS AND DISCUSSION

Here we apply the methods presented in the previous section in systems of graphene cylinders/tubes and metasurface-made cylinders, which are representative systems for the demonstration of the potential of our approaches, as well as systems associated with novel and engineerable optical properties.

A. Single scattering

1. Graphene cylinders

We begin our analysis by calculating the extinction efficiencies of (i) a single-layered and (ii) a double-layered cylinder, formed by homogeneous graphene layers. We assume that all the bulk cylinder layers are air, i.e., $\varepsilon_\ell = 1$ and $\mu_\ell = 1$, and the same for the host material. The geometry is comprised, in fact, of cocentered cylindrical cells/sheets with electric surface conductivity $\sigma_e = \sigma_g$ calculated using Eq. (1) and plotted in Fig. 2(a). (Such a geometry can be considered as a good approximation of a family of single- and double-wall carbon nanotubes.) The extinction efficiencies for a single graphene cylindrical layer of variable radius, $R = 35$, 45, and 55 nm, are shown in Fig. 3(a), while the extinction efficiencies for a double-layered cylinder with variable outer-layer radius R_2 are shown in Fig. 3(b). For the single graphene layer [Fig. 3(a)] there is only one dominant peak in the extinction spectrum, originated from the dipolar $\nu = 1$ mode for TE polarization. We denote this mode as TE_1 . Since,

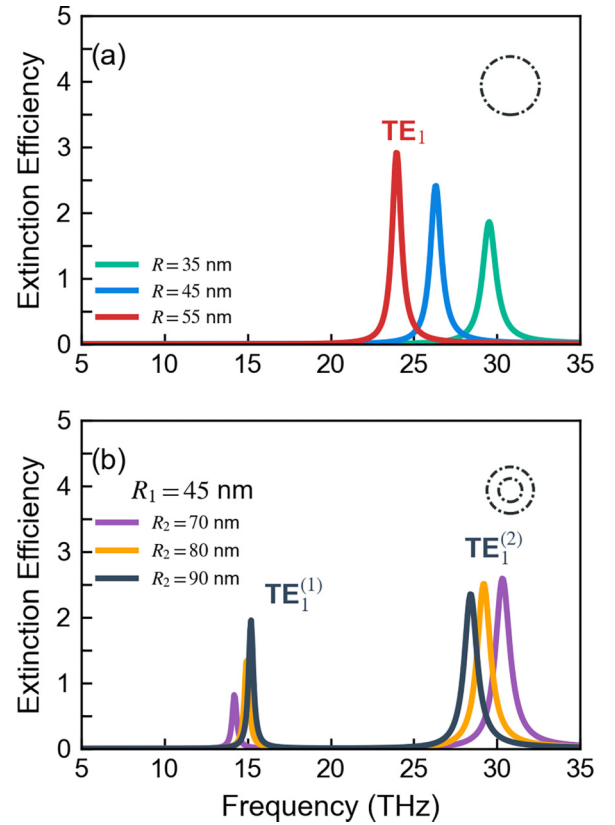


FIG. 3. Extinction efficiencies Q_{ext} in (a) a single-layer graphene cylindrical tube in air with varying radius R and (b) a double-layered graphene cylinder in air with inner radius $R_1 = 45$ nm, and variable outer layer radii R_2 for TE polarization. All layers exhibit surface conductivity σ_g with Fermi level $E_F = 0.2$ eV and relaxation time $\tau = 1$ ps. All cylinder bulk (inter-surface) layers are made of air.

in this frequency region the imaginary part of the surface conductivity of graphene [Fig. 2(a)] is positive, the mode is similar in nature to the localized surface plasmon resonance (LSPR) sustained in metallic rods [73].

For the double-layered case ($N = 2$) shown in Fig. 3(b), we consider a core of constant radius $R_1 = 45$ nm and the variable outer layer radius: $R_2 = 70$, 80, and 90 nm. In this case, the TE_1 mode manifests as two distinct resonances at frequencies below and above the TE_1 resonance for the single layer case. Here, we denote these resonances in order of increasing frequency as $\text{TE}_1^{(1)}$ and $\text{TE}_1^{(2)}$. From the frequency of the modes, one can conclude that the mode $\text{TE}_1^{(1)}$ comes predominately from the outer layer, redshifted due to the presence and interaction with the inner one, while $\text{TE}_1^{(2)}$ from the contribution of the core layer, blueshifted due to the interaction with the outer layer. A worth-mentioning feature of Fig. 3(b) is the small frequency shift of the $\text{TE}_1^{(1)}$ peak with the change of the radius R_2 , compared, e.g., with the corresponding shift observed in Fig. 3(a). The cause of this difference is the presence of the inner layer and the coupling between the two layers, as will be discussed also in the next paragraph. We should note here that for these systems the extinction efficiency for TM polarization is below 10^{-2} , with no resonances for both cases, and it is not shown here.

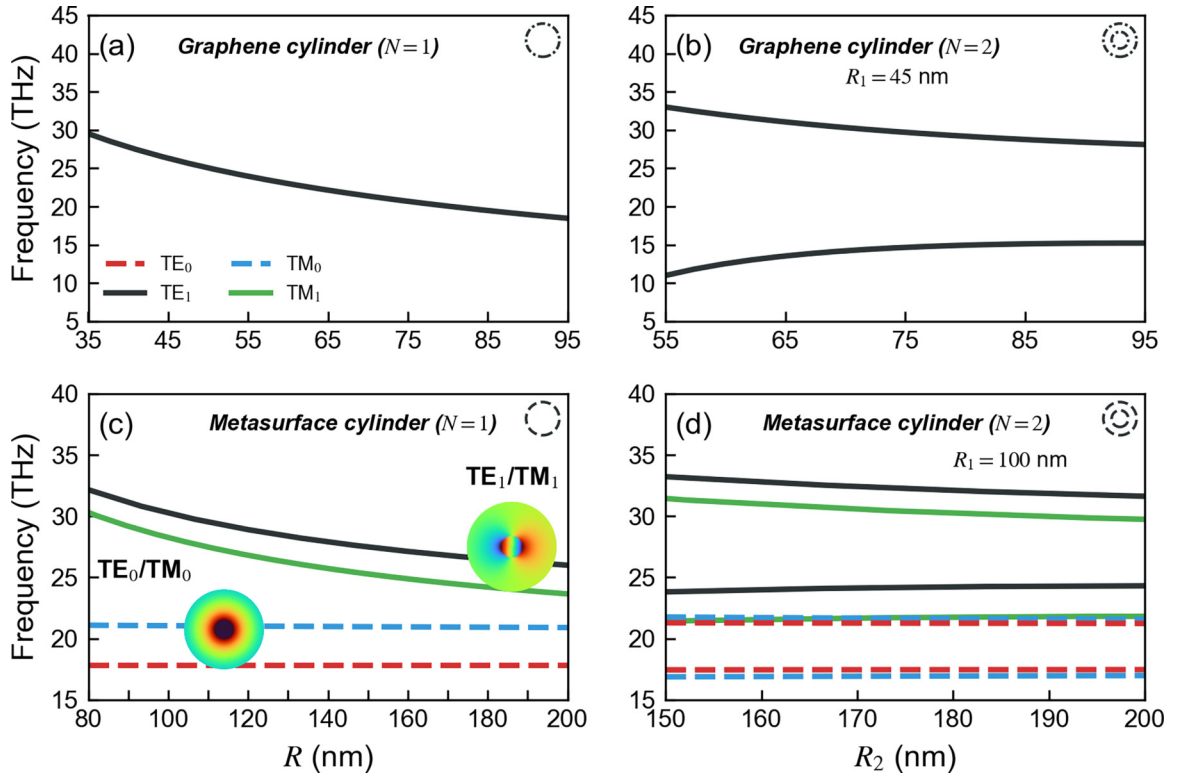


FIG. 4. Resonance frequencies of first two modes, $\nu = 0$ and $\nu = 1$, per polarization, TE and TM, for (a) a single-layered graphene cylinder versus its radius, R ; (b) a double-layered graphene cylinder for different outer-layer radii, R_2 and constant core radius $R_1 = 45$ nm; (c) a single-layered metasurface-formed cylinder of different radii, R ; (d) a double-layered metasurface cylinder with core radius $R_1 = 100$ nm and variable interlayer radii R_2 . The characteristic field distributions of the z component of the electric (magnetic) field for TM (TE) polarization for the $\nu = 0$ and $\nu = 1$ modes are shown in the insets of (c).

The dependence of the resonance frequencies on the radii of the graphene cylindrical layers, which are calculated by finding the poles of the scattering coefficients a_ν [Eq. (18)], are shown in Figs. 4(a) and 4(b). We observe that the resonance frequency in the single-layered cylinder scales with the radius of the cylinder with a $1/\sqrt{R}$ dependence as we derived in Eq. (28) (see Sec. II B). The tendency of TE_1 modes for the double-layered case ($N = 2$) can be explained in terms of mode hybridization and level repulsion, where the modes coupling leads to a lower-frequency “bonding” mode, redshifted in respect to the “parent” single-layer mode (with the shifting being larger for smaller difference between R_1 and R_2), and a higher frequency (antibonding) mode, blueshifted in respect to the corresponding single-layer mode [25,74–76]. Comparing the results of Figs. 4(a) and 4(b), we observe that the mode shifting due to the interaction of the inner and outer graphene layer is quite significant.

2. Metasurface cylinders

Next, we turn our attention to cylinders/tubes formed by metasurfaces having both electric and magnetic response, embedded in air. We consider two cases: (i) a single-layered metasurface-made cylinder of variable radius and (ii) a double-layered cylinder, of the same metasurface at each layer, with fixed inner-layer radius. The metasurfaces have resonant conductivities, $\sigma_{e(1)} = \sigma_{e(2)}$ and $\sigma_{m(1)} = \sigma_{m(2)}$ as it is shown in Fig. 2(b), and $\varepsilon_1 = \varepsilon_2 = \varepsilon_h = 1$. The extinction

efficiencies for both TE and TM polarizations and for the single- and the double-layered cylinders are shown in Fig. 5. In the single-layered cylinders, we investigate cases of radii $R = 50, 100,$ and 150 nm. There are two dominant resonances for both TE and TM polarizations. The electric in nature TM_0 and the magnetic in nature TE_0 modes appear just below the resonance frequencies of the electric sheet conductivity, $f_e = \omega_e/2\pi = 21$ THz, and the magnetic sheet conductivity, $f_m = \omega_m/2\pi = 18$ THz, respectively, and are practically independent of the cylinder radius. Just below f_e (f_m) the imaginary part of the electric (magnetic) sheet conductivity of the metasurface is negative [see Fig. 2(b)] leading to positive equivalent electrical permittivity (magnetic permeability); this case is similar to the polaritonic cylinders for small radii we have discussed in Ref. [64]. On the other hand, the dipolelike modes, TE_1 and TM_1 , fall in the regions of positive imaginary part of electric and magnetic conductivity respectively and they are similar in nature with the modes discussed earlier for the graphene case.

Next we study the case of the double-layered cylinder formed of the same metasurface, at inner layer radius $R_1 = 100$ nm and different outer layer radii R_2 . We observe two dipolar ($\nu = 1$) electric and magnetic modes, $TE_1^{(1)}$ and $TE_1^{(2)}$, $TM_1^{(1)}$ and $TM_1^{(2)}$, one of lower and one of higher frequency than the corresponding modes of a single-layered cylinder, similar in nature and behavior to the graphene case we discussed in the previous paragraph. Note here that the $TM_1^{(1)}$

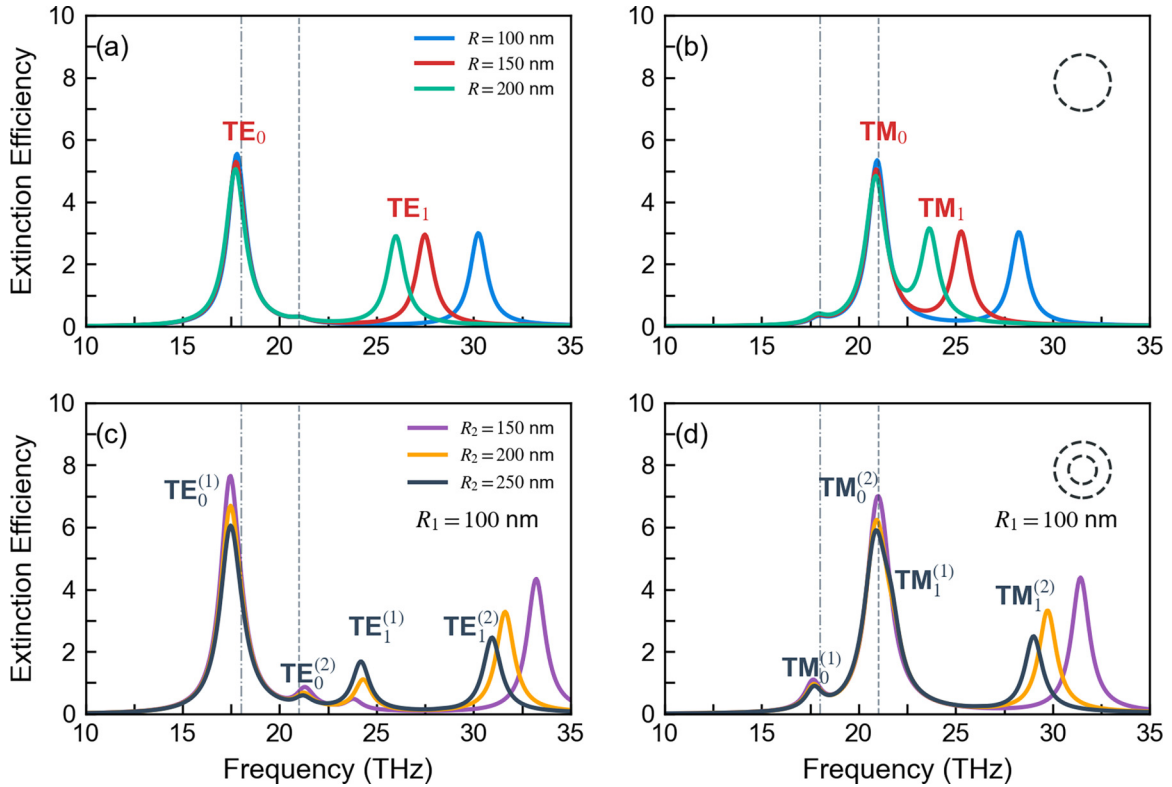


FIG. 5. Extinction efficiencies Q_{ext} for [(a) and (b)] a single-layered ($N = 1$) metasurface-formed cylinder of variable radius R for TE (a) and TM (b) polarization; [(c) and (d)] a double-layered ($N = 2$) metasurface cylinder with constant core radius $R_1 = 100$ nm and variable outer-layer radius, R_2 , for TE (c) and TM (d) polarization. The vertical dashed grey lines in the panels indicate the resonant frequencies of the metasurface magnetic and the electric conductivities at $f_m = 18$ THz and $f_e = 21$ THz, respectively. The symbols associated with each resonance are explained in the main text.

mode [see Fig. 4(d)] is very close in frequency with the $\text{TM}_0^{(2)}$ mode. Besides, there are the monopolar, $\nu = 0$, modes which are practically the same with the single-layer case, with main difference the enhancement of the extinction of the secondary peaks $\text{TE}_0^{(2)}$, $\text{TM}_0^{(2)}$, coinciding also with conductivities' resonances.

The dependence of the resonance frequencies of the dominant modes on the radius of the single-layered cylinder and on the radius R_2 for the double-layered case, for constant $R_1 = 100$ nm, is shown in Figs. 4(c) and 4(d). We observe that the $\nu = 1$ modes show similar behavior with the correspondent modes of the graphene case. The $\nu = 0$ modes on the other hand, where their originating field (electric for TM and magnetic for TE) does not encounter material discontinuities along its direction, almost coincide in frequency with the resonances of the conductivities and are unaffected by the cylinder radius.

It is interesting to observe though in the double-layer case the enhancement of the $\text{TE}_0^{(2)}$, $\text{TM}_0^{(2)}$ peaks compared to the single-layer case (where the peaks are hardly visible). To further elucidate this enhancement and the origin of those peaks we plot the zeroth-order scattering coefficients a_0 , in Fig. 6, for a double-layered cylinder with $R_1 = 100$ nm and $R_2 = 150$ nm as a function of the magnetic sheet conductivity resonance frequency, f_m , with constant $f_e = 21$ THz. For instance, for the TE polarization, we can observe that the strength of the weaker $\text{TE}_0^{(2)}$ resonance becomes more prominent and approaches in frequency the $\text{TE}_0^{(1)}$ as the res-

onance frequency f_m approaches f_e . Interestingly, even in the case of $f_e = f_m$, the two resonances remain distinct as a result of the interaction of the layers about the electric and magnetic conductivity resonance. However, the secondary TE_0 mode is absent when the electric conductivity is zero (see Fig. 12 in Appendix B 1), indicating that this dip corresponds to a magnetic mode originating from the resonant electric conductivity response, in analogy with the resonant magnetic response obtained in polaritonic or high-index dielectric cylinders, but of much smaller strength. Analogous behavior is observed in the case of the secondary TM_0 mode, which corresponds to electric response originated from large magnetism.

B. Effective medium theory and alternating optical phases

1. Graphene cylinders

We turn our attention now to the effective medium parameters ϵ_{eff} and μ_{eff} for clusters of graphene and metasurface cylinders in air, aligned in a square lattice, as presented in Fig. 1(c). The cylinders considered are the ones discussed in the previous section. We examine initially the graphene cases. In Fig. 7, we plot the real and imaginary parts of the tensor components of effective electric permittivity $\epsilon_{\text{eff}} = \epsilon_{\text{eff}}^{\perp}(\hat{x}\hat{x} + \hat{y}\hat{y}) + \epsilon_{\text{eff}}^{\parallel}\hat{z}\hat{z}$ for single-layered graphene cylinders [Figs. 7(a) and 7(c)] and double-layered cylinders [Figs. 7(b) and 7(d)] for constant filling ratio, $f = 20\%$, and different radii. As one can see, for both the single- and the double-layered

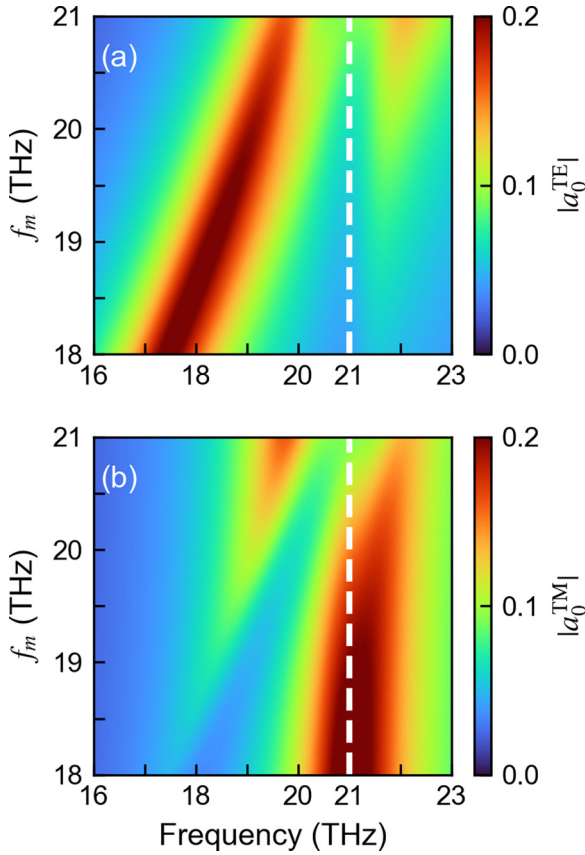


FIG. 6. Zeroth-order scattering coefficients, a_0 , as a function of the magnetic surface conductivity resonance frequency f_m for (a) TE and (b) TM polarizations for a double-layered metasurface cylinder ($N = 2$) with radii $R_1 = 100$ nm and $R_2 = 150$ nm, and constant electric surface conductivity resonance frequency $f_e = 21$ THz (dashed vertical line).

cases there are Lorentzian-shaped resonances for the in-plane component of the effective electric permittivity, $\epsilon_{\text{eff}}^{\perp}$, close in frequency to the corresponding TE_1 resonances [see Figs. 3, 4(a), and 4(b)]. Also we can observe a Drude-like response for the parallel component of effective electric permittivity $\epsilon_{\text{eff}}^{\parallel}$ for both arrays of single- and double-layered graphene cylinders. All the components of the effective magnetic permeability μ_{eff} are equal to unity and are not shown here. As the radius of the cylinders increases, the resonance of the $\epsilon_{\text{eff}}^{\perp}$ moves to lower frequencies. Interestingly, for single-layered cylinders all the components of the effective electric permittivity vanish at the same frequency, close to the TE_1 mode resonance frequency. For instance, for $R = 45$ nm the ϵ -near-zero (ENZ) is achieved at 23.7 THz and moves to lower frequencies as the radius of the cylinder increases. This result along with Eqs. (31) and (34) suggests that $a_0^{\text{TM}} = a_1^{\text{TE}}$ at that frequency for the single-layered graphene cylinder. Further examinations showed that the monochromatic vanishing of both components of effective permittivity tensor holds only for the symmetric case, where the material inside the graphene layer and the host are the same (air here). On the other hand, for the double-layered cylinders, due to the presence of multiple resonances, there are several frequencies where the $\epsilon_{\text{eff}}^{\perp}$ vanishes.

Moreover, as one can notice, there are frequency regions where the in-plane and out-of-plane components of the effective electric permittivity have different signs, i.e., $\epsilon_{\text{eff}}^{\perp} \cdot \epsilon_{\text{eff}}^{\parallel} < 0$. This is the condition for hyperbolic response (i.e., dispersion relation of the shape of hyperbola) for TM-polarized waves, as can be seen by taking into account the dispersion relations for an anisotropic homogeneous material [77],

$$\text{TM: } \frac{k_{\perp}^2}{\mu_{\text{eff}}^{\perp} \epsilon_{\text{eff}}^{\parallel}} + \frac{k_{\parallel}^2}{\mu_{\text{eff}}^{\parallel} \epsilon_{\text{eff}}^{\perp}} = \left(\frac{\omega}{c}\right)^2, \quad (39)$$

$$\text{TE: } \frac{k_{\perp}^2}{\mu_{\text{eff}}^{\parallel} \epsilon_{\text{eff}}^{\perp}} + \frac{k_{\parallel}^2}{\mu_{\text{eff}}^{\perp} \epsilon_{\text{eff}}^{\parallel}} = \left(\frac{\omega}{c}\right)^2, \quad (40)$$

where k_{\parallel} and k_{\perp} stand for the wave-vector components parallel and perpendicular to the cylinder axis respectively. For example, for the single-layered graphene cylinders with radius $R = 45$ nm [blue curve in Fig. 7(a)] the condition for hyperbolic response is achieved up to 28.6 THz, where both $\epsilon_{\text{eff}}^{\perp}$ and $\epsilon_{\text{eff}}^{\parallel}$ become positive. We can further distinguish the hyperbolic metamaterial response of our systems into two different frequency regions by considering the different signs of $\epsilon_{\text{eff}}^{\perp}$ and $\epsilon_{\text{eff}}^{\parallel}$. For frequencies below the $\epsilon_{\text{eff}}^{\perp}$ resonance (~ 24 THz), the in-plane components $\epsilon_{\text{eff}}^{\parallel}$ are positive, while the out-of-plane component $\epsilon_{\text{eff}}^{\perp}$ is negative; thus we have *type I hyperbolic metamaterial (HMM I)*. On the other hand, in the frequency region 24 THz–28.6 THz we have $\epsilon_{\text{eff}}^{\perp} < 0$ and $\epsilon_{\text{eff}}^{\parallel} > 0$, thus *hyperbolic metamaterial type II (HMM II)* response. The response is more rich for the metamaterial comprised of double-layered graphene cylinders shown in Figs. 7(b) and 7(d). Considering the case with constant core radius, $R_1 = 45$ nm, and variable outer layer radii, $R_2 = 70$ nm [green curve in Figs. 7(b) and 7(d)] and $R_2 = 90$ nm [purple curve in Figs. 7(b) and 7(d)], we see that there are alternating optical phases (HMM I, metallic, HMM II and dielectric) at frequencies close to the two TE_1 resonances. For instance, for $R_2 = 70$ nm, we find HMM I response in the frequency region up to 13.7 THz and 14.6–24.3 THz and HMM II response in the frequency region 28.5–32 THz.

We should mention also here that the response of graphene-shells and graphene-coated cylinders is highly tunable by changing the Fermi level of graphene. This, as mentioned, can be accomplished by various methods, including chemical doping, voltage tuning and photoexcitation. To assess the effect of this tunability on the effective properties of our graphene-based metamaterial we calculate first the dependence of the extinction efficiency on the graphene Fermi level, E_F , for a single-layered graphene cylinder, see Fig. 8(a). As observed in Fig. 8(a), the extinction efficiency is very small (maximum of $Q_{\text{ext}} = 0.05$) for the case of zero Fermi level; as the Fermi energy increases the extinction efficiency becomes larger and the resonance shifts to higher frequencies. Analogous trends are observed for the in-plane component of the effective electric permittivity $\epsilon_{\text{eff}}^{\perp}$, which is shown in Fig. 8(b). Figure 8(b) shows $\epsilon_{\text{eff}}^{\perp}$ for cylinders with radius $R = 45$ nm and filling ratio $f = 20\%$, for different Fermi energies, $E_F = 0, 0.1, 0.2, 0.3$, and 0.4 eV. The effective permittivity results are presented in parallel with single-scattering data [Fig. 8(a)], to facilitate the understanding of the observed response. We see that the TE_1 resonance of the single scattering setup [Fig. 8(a)] is moving

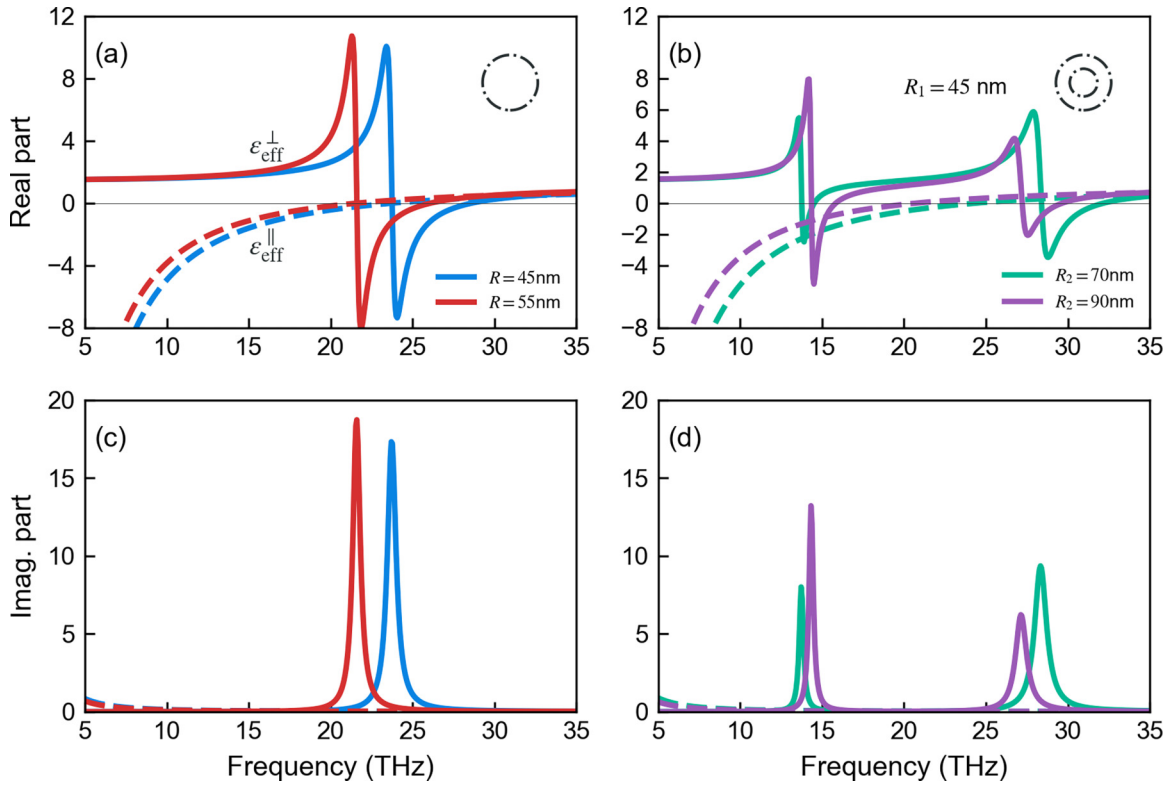


FIG. 7. Real (top) and imaginary (bottom) parts of the parallel $\epsilon_{\text{eff}}^{\parallel}$ (dashed curves) and perpendicular $\epsilon_{\text{eff}}^{\perp}$ (solid curves) components of the relative effective permittivity ϵ_{eff} for [(a) and (c)] a system made of single-layered ($N = 1$) graphene cylinders of variable radius, $R = 45$ nm (blue curves) and $R = 55$ nm (red curves) in air; [(b) and (d)] a system of double-layered ($N = 2$) graphene cylinders in air, with constant core radius $R_1 = 45$ nm, and for outer layer radii $R_2 = 70$ nm (green curves) and $R_2 = 90$ nm (purple curves); the cylinders filling ratio is in all cases equal to $f = 20\%$.

towards higher frequencies as the Fermi level grows, and the resonance becomes stronger in both extinction efficiency and effective electric permittivity spectra.

2. CPA accuracy

In order to verify and demonstrate the validity and accuracy of the developed effective medium approach, we compare its results with equivalent full-wave simulations data. Specifically we calculate the transmission and reflection spectra through a slab consisting of seven unit cells (along propagation direction) of a triple-layered ($N = 3$) graphene cylinder, in square arrangement, using the full wave numerical analysis software COMSOL MULTIPHYSICS, and we compare the results with the response (obtained by transfer matrix calculations) of a slab of the same thickness with electric permittivity ϵ_{eff} and magnetic permeability μ_{eff} calculated through our developed formalism. The transmission comparison for TE polarization is shown in Fig. 9. As can be seen, there is an excellent agreement between full wave simulations and the effective medium model. Moreover, in this particular system, the subwavelength size of the graphene tubes allows an accurate description by the CPA for frequencies even higher than the third structure resonance.

3. Metasurface-based cylinders

Next, we turn our attention to the effective response of arrays of metasurface-based cylinders, investigating the

single-layered and double-layered cylinder systems as previously; the results are presented in Figs. 10 and 11, respectively. The effective medium parameters for a single-layered cylinder metasurface for both TE and TM polarizations are shown in Fig. 10 for two cylinders radii, $R = 100$ nm (blue curves) and $R = 200$ nm (red curves). As one can notice in Fig. 10, the parallel components $\epsilon_{\text{eff}}^{\parallel}$ and $\mu_{\text{eff}}^{\parallel}$ (originating from the zero-th order modes) become resonant at the electric sheet conductivity and magnetic conductivity resonances of the constituent metasurfaces, respectively, while the change of radius only affects the strength of the resonant response. On the other hand, the perpendicular components, $\epsilon_{\text{eff}}^{\perp}$ and μ_{eff}^{\perp} , strongly depend, in both resonance frequency and strength, on the cylinder radius. The dependence of the resonance frequency follows the corresponding dependence of their “parent” single scattering modes TE_1 , TM_1 [see Figs. 5(a) and 5(b)] while the strength is favored from smaller radii.

Regarding the achievable metamaterial-related possibilities, we can observe that there are frequency regions where the medium becomes *double negative* (DNG) resulting in negative refractive index, i.e., both $\epsilon_{\text{eff}} < 0$ and its pertinent $\mu_{\text{eff}} < 0$. For $R = 100$ nm and TM polarization, both $\epsilon_{\text{eff}}^{\parallel}$ and μ_{eff}^{\perp} are negative between frequencies 28.19 and 28.64 THz. For the larger cylinder-radius system DNG is achieved for TM polarization, at lower frequencies, while for TE polarization there is no DNG response ($\epsilon_{\text{eff}}^{\perp} < 0$ and $\mu_{\text{eff}}^{\parallel} < 0$) for the parameters studied here.

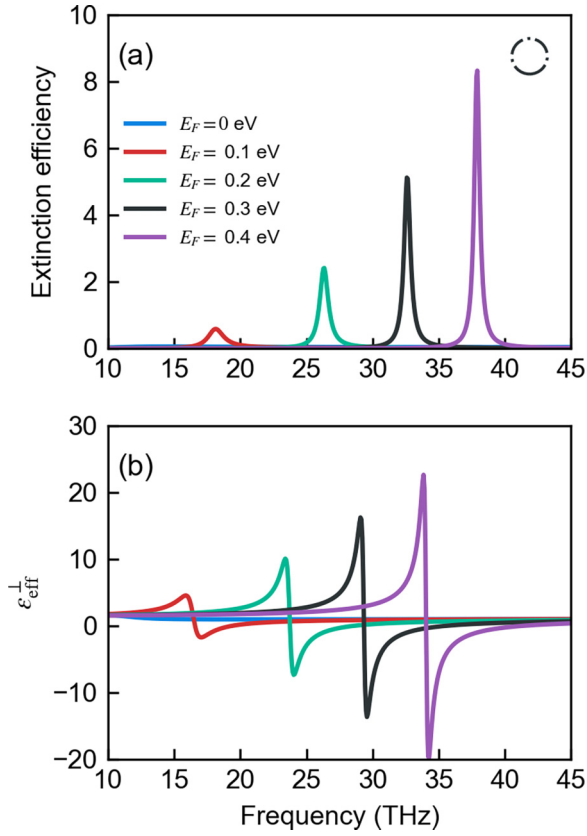


FIG. 8. (a) Extinction efficiency for TE polarization for a single-layered graphene cylinder with radius $R = 45$ nm in air, for different Fermi energies, E_F . (b) Real part of the in-plane component of effective electric permittivity $\epsilon_{\text{eff}}^{\perp}$ for a system of single-layered graphene cylinders as the one of panel (a), in air, with cylinder filling ratio $f = 20\%$.

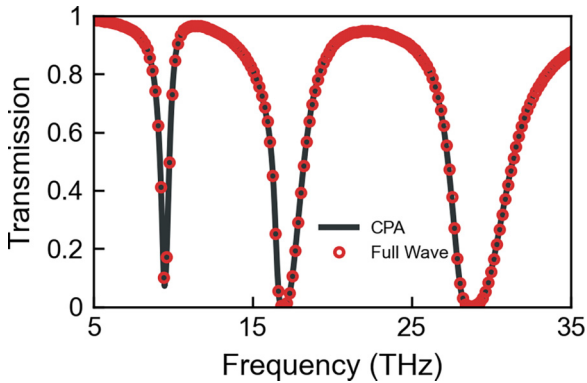


FIG. 9. Normal incidence, TE transmission spectra for a slab of triple-layered graphene cylinders with radii $R_1 = 45$ nm, $R_2 = 90$ nm, and $R_3 = 135$ nm and filling ratio $f = 20\%$ in air, in a square arrangement. The transmission is calculated by the commercial finite element method electromagnetic solver Comsol Multiphysics, considering a computational system of seven-unit-cell thickness (along the propagation direction). The full wave transmission results (red circles) are compared with results for a homogeneous effective medium of the same thickness as the actual system and effective parameters obtained through our CPA-based effective medium approach (black line).

It is interesting to observe also that the metasurface-cylinders system exhibits HMM response for both TM and TE polarizations. By considering the anisotropic material dispersion relations of Eqs. (39) and (40) and the results shown in Fig. 10 one can see that there are both HMM I and HMM II regions for both TM and TE polarizations. In particular, the arrays of metasurface-coated cylinders with $R = 100$ nm (blue curves in Fig. 10) and filling ratio $f = 20\%$ exhibit HMM I response ($\mu_{\text{eff}}^{\perp}\epsilon_{\text{eff}}^{\parallel} < 0$ and $\mu_{\text{eff}}^{\parallel}\epsilon_{\text{eff}}^{\perp} > 0$) in the frequency ranges 21.1–28.15 and 28.7–29.75 THz, and HMM II ($\mu_{\text{eff}}^{\perp}\epsilon_{\text{eff}}^{\parallel} > 0$ and $\mu_{\text{eff}}^{\parallel}\epsilon_{\text{eff}}^{\perp} < 0$) response in the frequency ranges 28.2–28.6 and 29.8–31.7 THz for TM polarization. Also, for TE polarization there is HMM I response ($\epsilon_{\text{eff}}^{\perp}\mu_{\text{eff}}^{\parallel} < 0$ and $\epsilon_{\text{eff}}^{\parallel}\mu_{\text{eff}}^{\perp} > 0$) in the frequency regions 17.97–26.53 and 28.75–29.75 THz, and HMM II response ($\epsilon_{\text{eff}}^{\perp}\mu_{\text{eff}}^{\parallel} > 0$ and $\epsilon_{\text{eff}}^{\parallel}\mu_{\text{eff}}^{\perp} < 0$) in the frequency range 28.19–28.7 THz.

We close our analysis by investigating the effective medium parameters for the double-layered metasurface cylinders systems, which are shown Fig. 11. We observe that for the parallel components $\epsilon_{\text{eff}}^{\parallel}$ and $\mu_{\text{eff}}^{\parallel}$ the presence of the second (outer) layer does not affect the resonance position. Regarding the resonance strength the outer layer seems to rather dominate or screen the response of the inner one. For the perpendicular components though we observe addition of resonances and “repulsion” of modes and in a way analogous to what was observed in the graphene case. As in the single-layered case we observe also here a rich electromagnetic response, with regions of alternating optical phase (between HMM I and HMM II) for both TE and TM polarizations. Regarding DNG response, although it is not observed in the results of Fig. 11, our calculations suggest that it can be achieved also for the double-layered case by properly tuning the structure parameters (radii, filling ratio).

IV. CONCLUSIONS

In this work, we derived analytically single scattering cross-sections and effective medium formulas for systems of multilayer cocentric cylinders. Every layer can be made of any material and can be coated with a metasurface of arbitrary resonant sheet-conductivities, both electric and magnetic. Starting from the investigation of the single cylinder’s scattering properties and resonances, for the formulation we combined Mie theory with a transfer matrix approach for cylindrical waves. The effective medium derivation was based on the coherent potential approximation method and provided semi-analytical expressions for the calculated effective medium parameters. Compared to commonly used effective medium approaches, the develop formulation is suitable also quite beyond the long-wavelength limit, is able to describe metamaterials made of resonant materials, predicts magnetism in all-dielectric media and accommodates cylindrical systems coated with resonant electromagnetic sheets.

We applied the formalism into two different metamaterial systems, operating in the technologically appealing THz region: (a) graphene nanotubes of one and two concentric layers (approximating systems of carbon nanotubes) and variable conductivity, and (b) nanotubes formed from a metasurface having both electric and magnetic response. We found that

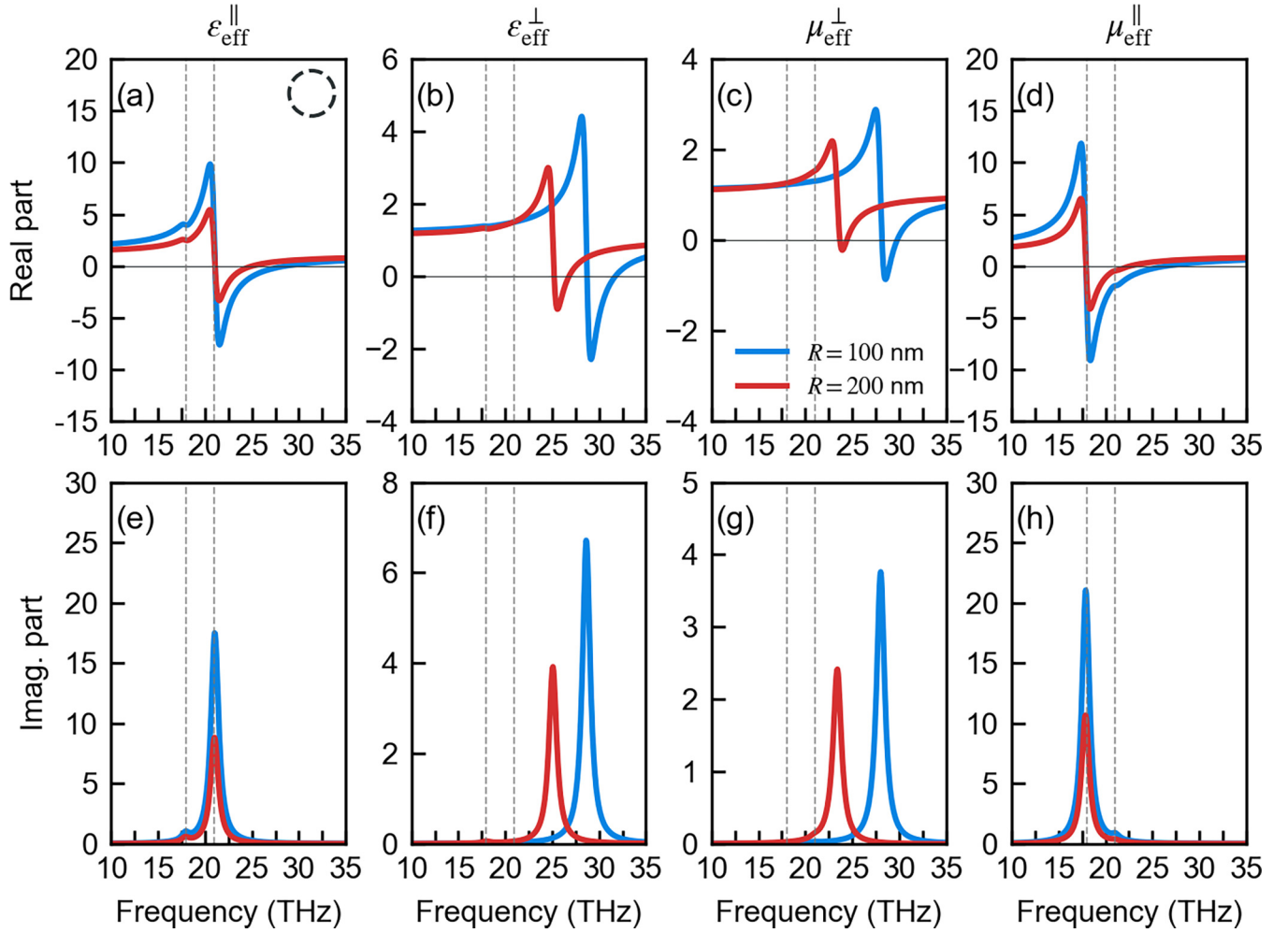


FIG. 10. Real (top) and imaginary (bottom) parts of the tensor components of effective permittivity ϵ_{eff} (first column $\epsilon_{\text{eff}}^{\parallel}$ and second column $\epsilon_{\text{eff}}^{\perp}$) and effective permeability μ_{eff} (third column μ_{eff}^{\perp} and fourth column $\mu_{\text{eff}}^{\parallel}$) for a system/metamaterial of single-layered ($N = 1$) metasurface-formed cylinders in air, for different radii, $R = 100$ nm (blue lines) and $R = 200$ nm (red lines), and filling ratio $f = 20\%$. The vertical dashed lines indicate the resonance frequencies of the magnetic ($f_m = 18$ THz) and electric sheet conductivity ($f_e = 21$ THz).

by properly choosing the number of layers and radii, both systems can exhibit a rich palette of electromagnetic response, own to the engineerable permittivity and permeability; this rich response includes hyperbolic behavior of both types I and II for both TE and TM polarizations, double negative response and regions of ϵ -near-zero and μ -near-zero response. Thus our results suggest that multilayer and metasurface-coated cylinders can be exploited for the design of multifunctional metamaterials and devices for the control of electromagnetic radiation, offering a vast range of possibilities, from super-scattering to cloaking and advanced wavefront manipulation.

ACKNOWLEDGMENTS

We acknowledge financial support by the European Union's Horizon 2020 FETOPEN programme under projects VISORSURF (Grant Agreement No. 736876), NANOPOLY (Grant Agreement No. 829061) and SMARTWAVE (Grant Agreement No. 952088) and by the General Secretariat for Research and Technology, and the H.F.R.I. Ph.D. Fellowship Grant (Grant Agreement No. 4894) in the context of the action

“1st Proclamation of Scholarships from ELIDEK for Ph.D. Candidates.”

APPENDIX A: TRANSFER MATRIX METHOD

In this Appendix, we derive the transfer matrices used in our analysis. For TE polarization the magnetic field is parallel to the cylinder axis, $\mathbf{H} = H_z \hat{z}$. The electric and magnetic fields in the ℓ th layer can be expanded on the basis of the cylindrical vector harmonics as

$$\mathbf{E}_\ell = i \sum_{v=-\infty}^{\infty} \frac{i^v}{k_\ell} [c_{\ell v} \mathbf{M}_{evk_\ell}^{(\text{outward})} + d_{\ell v} \mathbf{M}_{evk_\ell}^{(\text{inward})}], \quad (\text{A1})$$

$$\mathbf{H}_\ell = \frac{1}{\eta_\ell} \sum_{v=-\infty}^{\infty} \frac{i^v}{k_\ell} [c_{\ell v} \mathbf{N}_{evk_\ell}^{(\text{outward})} + d_{\ell v} \mathbf{N}_{evk_\ell}^{(\text{inward})}], \quad (\text{A2})$$

where c is the speed of light in vacuum, $k_\ell = \sqrt{\epsilon_\ell \mu_\ell} \frac{\omega}{c}$ and $\eta_\ell = \sqrt{\mu_\ell / \epsilon_\ell}$. The coefficients $c_{\ell v}$ and $d_{\ell v}$ can be determined from the boundary conditions at the surface of the cylinder.

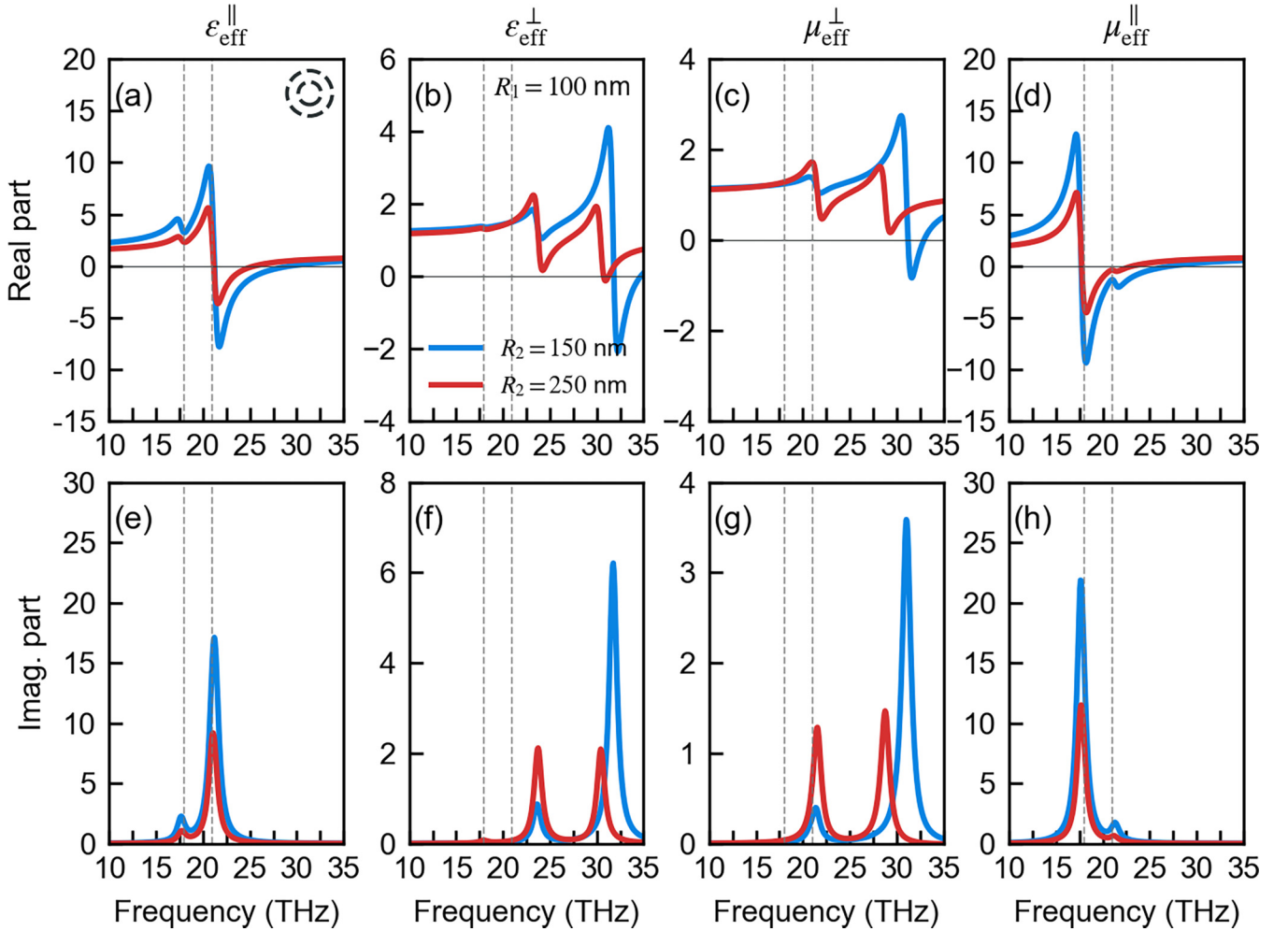


FIG. 11. Real (top) and imaginary (bottom) parts of the tensor components of effective permittivity ϵ_{eff} (first column $\epsilon_{\text{eff}}^{\parallel}$, second column $\epsilon_{\text{eff}}^{\perp}$) and effective permeability μ_{eff} (third column μ_{eff}^{\perp} , fourth column $\mu_{\text{eff}}^{\parallel}$) for a system/metamaterial of double-layered ($N = 2$) metasurface-formed cylinders in air, with core radius $R_1 = 100$ nm and for different outer-layer radii, $R_2 = 150$ nm (blue lines) and $R_2 = 250$ nm (red lines), and filling ratio $f = 20\%$. The vertical dashed lines indicate the resonance frequencies of the magnetic ($f_m = 18$ THz) and electric sheet conductivity ($f_e = 21$ THz).

The boundary conditions at the interface between the ℓ th and the $(\ell + 1)$ th layer (i.e., at $r = R_\ell$) can be written as

$$E_{\ell+1}^\varphi - E_\ell^\varphi = -\sigma_{m(\ell)} \frac{H_\ell^z + H_{\ell+1}^z}{2}, \quad (\text{A3})$$

$$H_{\ell+1}^z - H_\ell^z = -\sigma_{e(\ell)} \frac{E_\ell^\varphi + E_{\ell+1}^\varphi}{2}. \quad (\text{A4})$$

Using these conditions, we can connect the fields in the ℓ th and $(\ell + 1)$ th layers of the multilayer cylinder with a transfer matrix as

$$\mathbb{T}_{\ell v}^{\text{P}} \begin{pmatrix} d_{\ell v} \\ c_{(\ell+1),v} \end{pmatrix} = \begin{pmatrix} d_{(\ell+1),v} \\ c_{(\ell+1),v} \end{pmatrix}, \quad (\text{A5})$$

where $\mathbb{T}_{\ell v}^{\text{P}}$ is the transfer matrix for polarization $\text{P} = \text{TE}$.

For $\text{P} = \text{TM}$ polarization (the electric field is parallel to the cylinder axis, $\mathbf{E} = E_z \hat{z}$), the electric and magnetic fields in the ℓ th layer can be expanded as

$$\mathbf{H}_\ell = -\frac{i}{\eta_\ell} \sum_{\nu=-\infty}^{\infty} \frac{i^\nu}{k_\ell} [c_{\ell\nu} \mathbf{M}_{\nu k_\ell}^{(\text{outward})} + d_{\ell\nu} \mathbf{M}_{\nu k_\ell}^{(\text{inward})}], \quad (\text{A6})$$

$$\mathbf{E}_\ell = \sum_{\nu=-\infty}^{\infty} \frac{i^\nu}{k_\ell} [c_{\ell\nu} \mathbf{N}_{\nu k_\ell}^{(\text{outward})} + d_{\ell\nu} \mathbf{N}_{\nu k_\ell}^{(\text{inward})}]. \quad (\text{A7})$$

The boundary conditions between the ℓ th and the $(\ell + 1)$ th layers can be written as

$$E_{\ell+1}^z - E_\ell^z = \sigma_{m(\ell)} \frac{H_\ell^\varphi + H_{\ell+1}^\varphi}{2}, \quad (\text{A8})$$

$$H_{\ell+1}^\varphi - H_\ell^\varphi = \sigma_{e(\ell)} \frac{E_\ell^z + E_{\ell+1}^z}{2}. \quad (\text{A9})$$

APPENDIX B: EFFECTIVE MEDIUM THEORY

For the CPA configuration of Fig. 1(b), i.e., the coated multilayer cylinder embedded in the effective medium, the scattering coefficients can be derived through the equation for the total transfer matrix, which reads as

$$\mathbb{M}_{(N+1),\nu} \begin{pmatrix} b_\nu \\ 0 \end{pmatrix} = \begin{pmatrix} 1 \\ a_\nu^{(N+2)} \end{pmatrix}. \quad (\text{B1})$$

$\mathbb{M}_{(N+1),v}$ is the total transfer matrix of the layered infinitely long cylinder with $N + 1$ layers.

Therefore, the coefficient b_v and the scattering coefficient $a_v^{(N+2)}$ will be

$$b_v = \frac{1}{\mathbb{M}_{(N+1),v}^{(11)}}, \quad (\text{B2})$$

$$a_v^{(N+2)} = \mathbb{M}_{(N+1),v}^{(21)} b_v = \frac{\mathbb{M}_{(N+1),v}^{(21)}}{\mathbb{M}_{(N+1),v}^{(11)}}. \quad (\text{B3})$$

As stated in the main text, in order for an incoming wave to see a truly homogeneous medium, the scattering coefficient $a_v^{(N+2)}$ has to vanish (generalized CPA equation):

$$a_v^{(N+2)} = \mathbb{M}_{(N+1),v}^{(21)} b_v = \frac{\mathbb{M}_{(N+1),v}^{(21)}}{\mathbb{M}_{(N+1),v}^{(11)}} = 0, \quad (\text{B4})$$

which leads to

$$\mathbb{M}_{(N+1),v}^{(21)} = 0. \quad (\text{B5})$$

The above $\mathbb{M}_{(N+1),v}$ transfer matrix can be written as

$$\mathbb{M}_{(N+1),v} = \prod_{\ell=N+1}^1 \mathbb{T}_{\ell v} = \mathbb{T}_{(N+1),v} \prod_{\ell=N}^1 \mathbb{T}_{\ell v}. \quad (\text{B6})$$

For simplicity, we will denote $\mathbb{B}_{(N),v} = \prod_{\ell=N}^1 \mathbb{T}_{\ell v}$. This matrix contains information only about the original system. Using index notation for matrix multiplication $C^{ik} = \sum_j A^{ij} B^{jk}$, the generalized-CPA equation will be

$$\mathbb{M}_{(N+1),v}^{(21)} = 0 = \mathbb{T}_{(N+1),v}^{(21)} \mathbb{B}_{(N),v}^{(11)} + \mathbb{T}_{(N+1),v}^{(22)} \mathbb{B}_{(N),v}^{(21)} \quad (\text{B7})$$

or

$$-\frac{\mathbb{T}_{(N+1),v}^{(21)}}{\mathbb{T}_{(N+1),v}^{(22)}} = \frac{\mathbb{B}_{(N),v}^{(21)}}{\mathbb{B}_{(N),v}^{(11)}}. \quad (\text{B8})$$

For the term appearing in the left-hand side, we have $a_v(R_{N+1}; \text{eff}, h) = -\mathbb{T}_{(N+1),v}^{21} / \mathbb{T}_{(N+1),v}^{22}$, which is equal to the scattering coefficient of a single cylinder with electric permittivity ϵ_{eff} , magnetic permeability μ_{eff} and radius R_{N+1} embedded in a host with electric permittivity ϵ_h and magnetic permeability μ_{eff} . The right-hand side is equal to $a_v^{(N)} = \mathbb{B}_{(N),v}^{21} / \mathbb{B}_{(N),v}^{11}$ (scattering coefficient of N -layer cylinder in the host).

1. Extinction efficiencies for $N = 2$ and $\sigma_e = 0$ or $\sigma_m = 0$

Here we present the case of a double-layered cylinder coated with a metasurface of either $\sigma_e = 0$ or $\sigma_m = 0$. We keep $R_1 = 100$ nm, $f_e = 21$ THz, and $f_m = 18$ THz. The

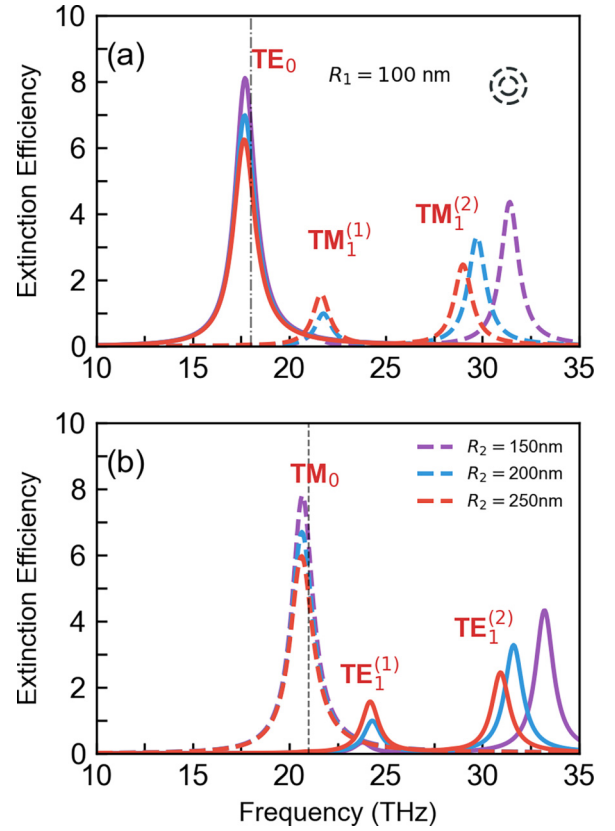


FIG. 12. TE (solid lines) and TM (dashed lines) extinction efficiencies for a double-layered metasurface-coated cylinder ($N = 2$) with core radius $R_1 = 100$ nm and various interlayer distances $\Delta_2 = R_2 - R_1$ for metasurfaces with (a) magnetic surface conductivity σ_m with $f_m = 18$ THz and $\sigma_e = 0$ and (b) electric surface conductivity σ_e with $f_e = 21$ THz and $\sigma_m = 0$. The vertical dashed grey lines indicate the resonances of the sheet conductivities.

extinction efficiencies are shown in Fig. 12. Comparing these results with Figs. 5(c) and 5(d) of the main text one can see several differences. Starting from the case with $\sigma_e = 0$ [Fig. 12(a)], we can see that the electric modes are absent from the extinction spectrum with only the magnetic modes TE_0 and TM_1 being present. Interestingly, while the two dipolar TM_1 modes observed in Fig. 5 remain also here, there is no the second TE_0 mode observed for the metasurface with nonzero σ_e and σ_m , verifying that this resonance corresponds to magnetic response in high index dielectrics. Analogous is the case of $\sigma_m = 0$ where only the electric TM_0 and TE_1 modes appear in the extinction spectrum.

- [1] X. Zhang and Z. Liu, Superlenses to overcome the diffraction limit, *Nat. Mater.* **7**, 435 (2008).
- [2] C. M. Soukoulis and M. Wegener, Past achievements and future challenges in the development of three-dimensional photonic metamaterials, *Nat. Photonics* **5**, 523 (2011).
- [3] Y. Lee, S.-J. Kim, H. Park, and B. Lee, Metamaterials and metasurfaces for sensor applications, *Sensors* **17**, 1726 (2017).

- [4] C. Liaskos, S. Nie, A. Tsioliariidou, A. Pitsillides, S. Ioannidis, and I. Akyildiz, A new wireless communication paradigm through software-controlled metasurfaces, *IEEE Commun. Mag.* **56**, 162 (2018).
- [5] C. M. Soukoulis, J. Zhou, T. Koschny, M. Kafesaki, and E. N. Economou, The science of negative index materials, *J. Phys.: Condens. Matter* **20**, 304217 (2008).

- [6] L. Peng, L. Ran, H. Chen, H. Zhang, J. A. Kong, and T. M. Grzegorzczak, Experimental Observation of Left-Handed Behavior in an Array of Standard Dielectric Resonators, *Phys. Rev. Lett.* **98**, 157403 (2007).
- [7] A. Kuznetsov, A. Miroshnichenko, M. Brongersma, Y. Kivshar, and B. Luk'yanchuk, Optically resonant dielectric nanostructures, *Science* **354**, aag2472 (2016).
- [8] Y. Kivshar, The rise of mie-tronics, *Nano Lett.* **22**, 3513 (2022).
- [9] L. Ferrari, C. Wu, D. Lepage, X. Zhang, and Z. Liu, Hyperbolic metamaterials and their applications, *Prog. Quantum Electron.* **40**, 1 (2015).
- [10] S. Liu, T. Cui, Q. Xu, D. Bao, L. Du, X. Wan, W. Tang, C. Ouyang, X. Zhou, H. Yuan, H. Ma, W. Jiang, J. Han, W. Zhang, and Q. Cheng, Anisotropic coding metamaterials and their powerful manipulation of differently polarized terahertz waves, *Light Sci. Appl.* **5**, e16076 (2016).
- [11] A. Basharin, C. Mavdis, M. Kafesaki, E. Economou, and C. Soukoulis, Epsilon near zero based phenomena in metamaterials, *Phys. Rev. B* **87**, 155130 (2013).
- [12] I. Katsantonis, S. Droulias, C. M. Soukoulis, E. N. Economou, and M. Kafesaki, Pt-symmetric chiral metamaterials: Asymmetric effects and pt-phase control, *Phys. Rev. B* **101**, 214109 (2020).
- [13] S. Glybovski, S. Tretyakov, P. Belov, Y. Kivshar, and C. Simovski, Metasurfaces: From microwaves to visible, *Phys. Rep.* **634**, 1 (2016).
- [14] M. Chen, M. Kim, A. M. Wong, and G. V. Eleftheriades, Huygens' metasurfaces from microwaves to optics: A review, *Nanophotonics* **7**, 1207 (2018).
- [15] M. Beruete and I. Jáuregui-López, Terahertz sensing based on metasurfaces, *Adv. Opt. Mater.* **8**, 1900721 (2020).
- [16] A. C. Tasolamprou, L. Zhang, M. Kafesaki, T. Koschny, and C. M. Soukoulis, Experimentally excellent beaming in a two-layer dielectric structure, *Opt. Express* **22**, 23147 (2014).
- [17] E. Skoulas, A. C. Tasolamprou, G. Kenanakis, and E. Stratakis, Laser induced periodic surface structures as polarizing optical elements, *Appl. Surf. Sci.* **541**, 148470 (2021).
- [18] A. C. Tasolamprou, E. Skoulas, G. Perrakis, M. Vlahou, Z. Viskadourakis, E. N. Economou, M. Kafesaki, G. Kenanakis, and E. Stratakis, Highly ordered laser imprinted plasmonic metasurfaces for polarization sensitive perfect absorption, *Sci. Rep.* **12**, 19769 (2022).
- [19] H. Zhu, Q. Li, C. Tao, Y. Hong, Z. Xu, W. Shen, S. Kaur, P. Ghosh, and M. Qiu, Multispectral camouflage for infrared, visible, lasers and microwave with radiative cooling, *Nat. Commun.* **12**, 1805 (2021).
- [20] G. Perrakis, A. C. Tasolamprou, G. Kenanakis, E. Economou, S. Tzortzakis, and M. Kafesaki, Combined nano and micro structuring for enhanced radiative cooling and efficiency of photovoltaic cells, *Sci. Rep.* **11**, 11552 (2021).
- [21] G. Perrakis, A. C. Tasolamprou, G. Kenanakis, E. N. Economou, S. Tzortzakis, and M. Kafesaki, Submicron organic-inorganic hybrid radiative cooling coatings for stable, ultrathin, and lightweight solar cells, *ACS Photonics* **9**, 1327 (2022).
- [22] Z. Ruan and S. Fan, Superscattering of Light from Sub-wavelength Nanostructures, *Phys. Rev. Lett.* **105**, 013901 (2010).
- [23] S. Lepeshov, A. Krasnok, and A. Alù, Nonscattering-to-Superscattering Switch with Phase-Change Materials, *ACS Photonics* **6**, 2126 (2019).
- [24] H.-W. Wu, Y. Fang, J.-Q. Quan, Y.-Z. Han, Y.-Q. Yin, Y. Li, and Z.-Q. Sheng, Multifrequency superscattering with high Q factors from a deep-subwavelength spoof plasmonic structure, *Phys. Rev. B* **100**, 235443 (2019).
- [25] S. H. Raad, C. J. Zapata-Rodríguez, and Z. Atlasbaf, Graphene-coated resonators with frequency-selective super-scattering and super-cloaking, *J. Phys. D: Appl. Phys.* **52**, 495101 (2019).
- [26] S. H. Raad, C. J. Zapata-Rodríguez, and Z. Atlasbaf, Multifrequency super-scattering from sub-wavelength graphene-coated nanotubes, *J. Opt. Soc. Am. B* **36**, 2292 (2019).
- [27] A. Abrashuly and C. Valagiannopoulos, Limits for Absorption and Scattering by Core-Shell Nanowires in the Visible Spectrum, *Phys. Rev. Appl.* **11**, 014051 (2019).
- [28] A. Alù and N. Engheta, Achieving transparency with plasmonic and metamaterial coatings, *Phys. Rev. E* **72**, 016623 (2005).
- [29] H. M. Bernety and A. B. Yakovlev, Cloaking of single and multiple elliptical cylinders and strips with confocal elliptical nanostructured graphene metasurface, *J. Phys.: Condens. Matter* **27**, 185304 (2015).
- [30] L. Zhang, Y. Shi, and C.-H. Liang, Optimal illusion and invisibility of multilayered anisotropic cylinders and spheres, *Opt. Express* **24**, 23333 (2016).
- [31] M. Naserpour, C. J. Zapata-Rodríguez, S. M. Vuković, H. Pashaeiadi, and M. R. Belić, Tunable invisibility cloaking by using isolated graphene-coated nanowires and dimers, *Sci. Rep.* **7**, 12186 (2017).
- [32] G. Labate, A. Alù, and L. Matekovits, Surface-admittance equivalence principle for nonradiating and cloaking problems, *Phys. Rev. A* **95**, 063841 (2017).
- [33] S. Batool, M. Nisar, F. Frezza, and F. Mangini, Cloaking Using the Anisotropic Multilayer Sphere, *Photonics* **7**, 52 (2020).
- [34] V. I. Shcherbinin, V. I. Fesenko, T. I. Tkachova, and V. R. Tuz, Superscattering from subwavelength corrugated cylinders, *Phys. Rev. Appl.* **13**, 024081 (2020).
- [35] K. Zheng, Z. Zhang, F. Qin, and Y. Xu, Invisible Mie scatterer, *Opt. Lett.* **46**, 5248 (2021).
- [36] J. A. Lock, Scattering of an electromagnetic plane wave by a Luneburg lens III Finely stratified sphere model, *J. Opt. Soc. Am. A* **25**, 2991 (2008).
- [37] R. Kumar and K. Kajikawa, Superscattering from cylindrical hyperbolic metamaterials in the visible region, *Opt. Express* **28**, 1507 (2020).
- [38] T. Kaplas and P. Kuzhir, Ultra-thin pyrocarbon films as a versatile coating material, *Nanoscale Res. Lett.* **12**, 121 (2017).
- [39] P. Kuzhir, A. Paddubskaya, D. Bychanok, A. Liubimau, A. Ortona, V. Fierro, and A. Celzard, 3d-printed, carbon-based, lossy photonic crystals: Is high electrical conductivity the must? *Carbon* **171**, 484 (2021).
- [40] M. Shuba, D. Yuko, P. Kuzhir, S. Maksimenko, V. Ksenevich, S.-H. Lim, T.-H. Kim, and S.-M. Choi, Electromagnetic and optical responses of a composite material comprising individual single-walled carbon-nanotubes with a polymer coating, *Sci. Rep.* **10**, 9361 (2020).
- [41] O. Sedelnikova, D. Gorodetskiy, A. Kurennya, K. Baskakova, E. Shlyakhova, A. Makarova, G. Gorokhov, D. Bychanok, P. Kuzhir, S. Maksimenko, L. Bulusheva, and A. Okotrub, Laser patterning of aligned carbon nanotubes arrays: Morphology, surface structure, and interaction with terahertz radiation, *Materials* **14**, 3275 (2021).

- [42] P.-Y. Chen, J. Soric, Y. R. Padooru, H. M. Bernety, A. B. Yakovlev, and A. Alù, Nanostructured graphene metasurface for tunable terahertz cloaking, *New J. Phys.* **15**, 123029 (2013).
- [43] T. Christensen, A.-P. Jauho, M. Wubs, and N. A. Mortensen, Localized plasmons in graphene-coated nanospheres, *Phys. Rev. B* **91**, 125414 (2015).
- [44] T. I. Tkachova, V. I. Shcherbinin, and V. I. Tkachenko, Selectivity properties of cylindrical waveguides with longitudinal wall corrugations for second-harmonic gyrotrons, *J Infrared Milli. Terahz. Waves* **40**, 1021 (2019).
- [45] Q. Qian, Y. Yan, and C. Wang, Flexible metasurface black nickel with stepped nanopillars, *Opt. Lett.* **43**, 1231 (2018).
- [46] A. C. Tasolamprou, D. Mentzaki, Z. Viskadourakis, E. Economou, M. Kafesaki, and G. Kenanakis, Flexible 3D printed conductive metamaterial units for electromagnetic applications in microwaves, *Materials* **13**, 3879 (2020).
- [47] G. Yao, F. Ling, J. Yue, C. Luo, J. Ji, and J. Yao, Dual-band tunable perfect metamaterial absorber in the THZ range, *Opt. Express* **24**, 1518 (2016).
- [48] A. C. Tasolamprou, A. Koulouklidis, C. Daskalaki, C. P. Mavidis, G. Kenanakis, G. Deligeorgis, Z. Viskadourakis, P. Kuzhir, S. Tzortzakis, M. Kafesaki, E. Economou, and C. Soukoulis, Experimental demonstration of ultrafast THZ modulation in a graphene-based thin film absorber through negative photoinduced conductivity, *ACS Photonics* **6**, 720 (2019).
- [49] A. Ahmadvand, B. Gerislioglu, and Z. Ramezani, Gated graphene island-enabled tunable charge transfer plasmon terahertz metamodulator, *Nanoscale* **11**, 8091 (2019).
- [50] A. D. Koulouklidis, A. C. Tasolamprou, S. Doukas, E. Kyriakou, M. S. Ergoktas, C. Daskalaki, E. N. Economou, C. Kocabas, E. Lidorikis, M. Kafesaki, and S. Tzortzakis, Ultrafast terahertz self-induced absorption and phase modulation on a graphene-based thin film absorber, *ACS Photonics* **9**, 3075 (2022).
- [51] S. Yan and G. A. E. Vandenbosch, Increasing the NRI bandwidth of dielectric sphere-based metamaterials by coating, *Prog. Electromagn. Res.* **132**, 1 (2012).
- [52] H.-Y. She, L.-W. Li, O. J. F. Martin, and J. R. Mosig, Surface polaritons of small coated cylinders illuminated by normal incident TM and TE plane waves, *Opt. Express* **16**, 1007 (2008).
- [53] A. Alù, Mantle cloak: Invisibility induced by a surface, *Phys. Rev. B* **80**, 245115 (2009).
- [54] M. Danaeifar and N. Granpayeh, Wideband invisibility by using inhomogeneous metasurfaces of graphene nanodisks in the infrared regime, *J. Opt. Soc. Am. B* **33**, 1764 (2016).
- [55] E. Shokati, N. Granpayeh, and M. Danaeifar, Wideband and multi-frequency infrared cloaking of spherical objects by using the graphene-based metasurface, *Appl. Opt.* **56**, 3053 (2017).
- [56] Z. Hamzavi-Zarghani, A. Yahaghi, L. Matekovits, and A. Farmani, Tunable mantle cloaking utilizing graphene metasurface for terahertz sensing applications, *Opt. Express* **27**, 34824 (2019).
- [57] P. Tassin, T. Koschny, and C. M. Soukoulis, Effective material parameter retrieval for thin sheets: Theory and application to graphene, thin silver films, and single-layer metamaterials, *Phys. B: Condens. Matter* **407**, 4062 (2012).
- [58] O. Tsilipakos, T. Koschny, and C. M. Soukoulis, Antimatched electromagnetic metasurfaces for broadband arbitrary phase manipulation in reflection, *ACS Photonics* **5**, 1101 (2018).
- [59] S. Droulias, Chiral sensing with achiral isotropic metasurfaces, *Phys. Rev. B* **102**, 075119 (2020).
- [60] M. Kafesaki and E. N. Economou, Acoustic waves in random media, *Europhys. Lett.* **37**, 7 (1997).
- [61] M. Kafesaki and E. N. Economou, Acoustic and elastic waves in random media - CPA, *Annalen der Physik* **510**, 383 (1998).
- [62] Y. Wu, J. Li, Z.-Q. Zhang, and C. T. Chan, Effective medium theory for magnetodielectric composites: Beyond the long-wavelength limit, *Phys. Rev. B* **74**, 085111 (2006).
- [63] P. Sheng, *Introduction to Wave Scattering, Localization and Mesoscopic Phenomena*, Springer Series in MATERIALS SCIENCE, Vol. 88 (Springer Berlin Heidelberg, Berlin, Heidelberg, 2006).
- [64] C. P. Mavidis, A. C. Tasolamprou, E. N. Economou, C. M. Soukoulis, and M. Kafesaki, Polaritonic cylinders as multifunctional metamaterials: Single scattering and effective medium description, *Phys. Rev. B* **102**, 155310 (2020).
- [65] L. A. Falkovsky and A. A. Varlamov, Space-time dispersion of graphene conductivity, *Eur. Phys. J. B* **56**, 281 (2007).
- [66] Y. Ra'di, V. S. Asadchy, and S. A. Tretyakov, Tailoring Reflections From Thin Composite Metamirrors, *IEEE Trans. Antennas Propag.* **62**, 3749 (2014).
- [67] N. Mohammadi Estakhri and A. Alù, Wave-front Transformation with Gradient Metasurfaces, *Phys. Rev. X* **6**, 041008 (2016).
- [68] J. A. Stratton, *Electromagnetic Theory* (John Wiley & Sons, Inc., Hoboken, NJ, USA, 2015).
- [69] E. Kuester, M. Mohamed, M. Piket-May, and C. Holloway, Averaged transition conditions for electromagnetic fields at a metafilm, *IEEE Trans. Antennas Propag.* **51**, 2641 (2003).
- [70] C. L. Holloway, E. F. Kuester, and A. Dienstfrey, Characterizing metasurfaces/metafilms: the connection between surface susceptibilities and effective material properties, *IEEE Antennas Wirel. Propag. Lett.* **10**, 1507 (2011).
- [71] M. Dehmollaian, N. Chamanara, and C. Caloz, Wave scattering by a cylindrical metasurface cavity of arbitrary cross section: Theory and applications, *IEEE Trans. Antennas Propag.* **67**, 4059 (2019).
- [72] M. Abramowitz, I. A. Stegun, and D. Miller, *Handbook of Mathematical Functions With Formulas, Graphs and Mathematical Tables* (United States Department of Commerce, National Institute of Standards and Technology (NBS), Washington D.C., 1964).
- [73] C. A. Pfeiffer, E. N. Economou, and K. L. Ngai, Surface polaritons in a circularly cylindrical interface: Surface plasmons, *Phys. Rev. B* **10**, 3038 (1974).
- [74] E. Prodan, C. Radloff, N. J. Halas, and P. Nordlander, A hybridization model for the plasmon response of complex nanostructures, *Science* **302**, 419 (2003).
- [75] W. Liu, R. F. Oulton, and Y. S. Kivshar, Geometric interpretations for resonances of plasmonic nanoparticles, *Sci. Rep.* **5**, 12148 (2015).
- [76] R. Li, B. Zheng, X. Lin, R. Hao, S. Lin, W. Yin, E. Li, and H. Chen, Design of Ultracompact Graphene-Based Superscatterers, *IEEE J. Sel. Top. Quantum Electron.* **23**, 130 (2017).
- [77] R. A. Depine, M. E. Inchaussandague, and A. Lakhtakia, Classification of dispersion equations for homogeneous, dielectric-magnetic, uniaxial materials, *J. Opt. Soc. Am. A* **23**, 949 (2006).